THESIS

Reconstructing HI power spectrum using dark matter distribution

暗黒物質分布を用いた
HIパワースペクトルの再構築

Rika Ando

Division of Particle and Astrophysical Science, Nagoya University

March 2022

Abstract

Currently, our Universe is accelerated expanding. The dark matter alone under general relativity cannot explain this accelerating expansion. Therefore, various theoretical models have been proposed, such as dark energy or the modified gravity theory, extending general relativity on large scales. The differences between these theoretical models appear as differences in the time evolution of the density fluctuations of matter on large scales and the expansion history of the Universe. Therefore, exploration of the large-scale structure of the Universe is a powerful tool to determine the origin of the accelerating expansion. Although galaxies have been used as tracers of dark matter, the 21cm line, which is emitted from neutral hydrogen due to the hyperfine structure, is expected to be used for future observations. However, the theoretical model of 21cm clustering has not been sufficiently developed for comparison with observations. We need to develop a theoretical model of the large-scale clustering of spatial fluctuations in the 21cm line signal to constrain the cosmology accurately.

This thesis proposes a new method to generate the distribution of neutral hydrogen from N-body simulations, which calculate only the gravitational interaction of dark matter. In this thesis, data from publicly available cosmological hydrodynamic simulations are used. First, I compared the power spectra of dark matter and neutral hydrogen to see the difference in their distributions. I obtained the neutral hydrogen distribution from the mass and the neutral fraction of gas particles, and this was assumed to be the ”true” neutral hydrogen distribution. As a result, I find that most of the neutral hydrogen existed in the sphere of about three times the radius from the center of the dark matter halo, and thus I need to consider the outside of the halo.

Next, I proposed a method to generate the neutral hydrogen distribution from the dark matter distribution and reproduce the slope of the neutral hydrogen power spectrum on the large-scale side. This method first uses only the density field of dark matter inside a sphere of constant radius times the center of the dark matter halo and sets the density outside to zero. I get the two times of the halo radius best reproduces the slope of the neutral hydrogen power spectrum by comparing the slope of the neutral hydrogen power spectrum with the reconstructed one. O also show that spin-temperature fluctuations modify the amplitude of the 21-cm line power spectrum by up to 8% at redshift 3.

Acknowledgements

First of all, I would like to express my sincere gratitude to my supervisor, Kiyotomo Ichiki, for his support and encouragement in my research. He is one of my motivations to join the laboratory, and he makes my research life more enjoyable. I would also like to thank Atsushi J. Nishizawa for the discussions as a co-researcher and teaching me how to present our studies effectively. I am also grateful to Hiroyuki Tashiro and Kenji Hasegawa for their helpful advice on the physics of the 21-cm line and the galaxies.

I would like to express my gratitude to thank Prof. Naoshi Sugiyama, PI in the cosmology group at Nagoya University, C-lab, for teaching me how to think and study physics and cosmology. I would also like to thank my co-researchers, Kentaro Nagamine and Ikko Shimizu, for taking the regular discussions and giving me professional advice. I would also thank all staff members and students of C-lab for many valuable discussions and advice. In particular, thanks to Kazuhiro Kogai and Daiki Hashimoto, the Ph.D. course was enjoyable for me. I would also like to thank secretaries in C-lab, Mio Kato and Hitomi Tanaka, for always helping me with desk works.

Finally, I am very grateful to my family and friends for motivating and supporting me.

Contents

Chapter 1

Introduction

1.1 Accelerating Expansion of the Universe

Since Einstein thought that the Universe was static, he added the cosmological constant Λ in general relativity to make a static universe in 1917. However, in 1922, Friedmann predicted a model of an expanding Universe by applying general relativity to the Universe (Friedmann, 1922). Furthermore, in 1929, Lemaitre also predicted a solution for the expanding Universe and suggested that the redshift of the galaxies was due to the expansion of the Universe (Lemaître, 1927). In 1929, Hubble revealed the expansion of the Universe through observations of the relationship between the recession velocity of galaxies and distance to them (Hubble, 1929). The observation showed a linear relationship between recession velocity and distance for nearby galaxies, and the more distant the galaxy, the faster it appears to move away.

In the 1990s, the observations of Type Ia supernovae by Riess et al. (1998) and Perlmutter et al. (1999) revealed that the current expansion of the Universe is accelerating. However, the Universe with only the ordinary matter under general relativity should be a decelerating expansion and not cause an accelerating expansion. Then, dark energy has been proposed as unknown energy that exerts a repulsive force on the Universe. The observation of the cosmic microwave background (CMB) showed that dark energy accounts for about 69% of the energy density of the Universe (Planck Collaboration et al., 2020).

In general relativity, acceleration of the expansion of the Universe is described by

$$\frac{\ddot{a}}{a} = -4\pi G\rho \left(w + \frac{1}{3} \right), \tag{1.1}$$

where $w = p/\rho$ is the equation of state parameter representing the ratio of the pressure to the density and G is gravitational constant. $a = a(t)$ is a scale factor of the Universe and represents the relative size of the Universe. $\ddot{a}/a$ means

the acceleration of the time variation of the size of the Universe and is positive when the Universe is accelerating expanding. Although dark matter has $w = 0$ and radiation has $w = 1/3$, w must be less than $-1/3$ for accelerating expansion. Thus, dark energy is a candidate for the origin of the accelerating expansion of the Universe. Cosmological constant Λ is one of the dark energy models and its equation of state parameter is $w = -1$. The cosmological constant is thought to be the vacuum energy. However, the theoretical prediction of energy density for vacuum energy has 120 orders of magnitude larger than that obtained by observations of accelerated expansion. The origin of the accelerating expansion is still one of the key issues in cosmology. The science goal of this thesis is also to distinguish whether dark energy is a cosmological constant or not.

1.2 Standard ruler

Differences in dark energy models appear in differences in the expansion history of the Universe and in the time evolution of density fluctuations. The expansion history of the Universe has been explored mainly by two methodologies. The dark energy study using Type Ia supernovae is based on a method to estimate the redshift-distance relation from the apparent brightness of an object with a known brightness, and is still being investigated intensively. Recently, the method of estimating the redshift-distance relation from the apparent angular size on the celestial sphere of an object with known physical size has attracted much attention.

Baryon Acoustic Oscillation (BAO) is such a structure whose characteristic size is known. In the early Universe, the Universe was filled with hot, dense plasma. By Thomson scattering, photons interacted with free electrons, and nuclei interacted with free electrons by Coulomb forces. Thereby, photons and baryons were strongly coupled. This single fluid was acoustic oscillating due to photon pressure in the gravitational potential by the dark matter. As the Universe expands and cools down, the photon-baryon coupling breaks, allowing the photons to travel freely. We observe these photons as the CMB. At the same time, acoustic oscillations of baryons are frozen and imprinted on the density distribution. The characteristic scale of BAO is the acoustic horizon at decoupling r_s, which is about 150Mpc. It has been precisely measured from CMB observations.

Density fluctuations grow gravitationally, and BAO remain in the large-scale structure of the Universe. We can see the BAO feature in the current distribution of distances between galaxies. The BAO feature appears in the two-point correlation function and power spectrum. We can measure the distance to the BAO by comparing the apparent size of the BAO with the ac-

tual size. Precisely, angular distance is constrained by the perspective angle and the Hubble parameter from the difference in redshift along the line-of-sight. Another approach is the Alcock Paczyński (AP) test (Lepori et al., 2017), which uses the isotropic structure of BAO to constrain the cosmological model so that the size in the line-of-sight and that in angular directions are equal. Note that dark matter, the main component of the matter, cannot be observed with electromagnetic waves; therefore, it is necessary to observe the large-scale structure and BAO using tracer such as galaxies.

Eisenstein et al. (2005) reported the first detection of BAO signals in luminous red galaxies (LRG) two-point correlation function obtained by the Sloan Digital Sky Survey (SDSS). Recent studies showed that using the BAO data alone can suggest the existence of cosmological constant Λ at $> 6.6\sigma$ significance (Ata et al., 2018a). Conventional BAO analysis is mainly based on galaxy surveys (Beutler et al., 2011; Ross et al., 2015; Gil-Marín et al., 2020). In addition, observations of quasi-stellar objects (QSOs) (Ata et al., 2018b; Zarrouk et al., 2021) and Lyman-alpha forest (du Mas des Bourboux et al., 2020) are also used.

1.3 21-cm line intensity mapping survey

In the coming decade, BAO analysis using neutral hydrogen (HI) as a tracer of the large-scale structure will start. By the spin-flip transition between the proton and the electron, HI emits radio waves whose rest-frame wavelength is 21 cm, corresponding to the energy difference in the hyperfine structure. Therefore we call this electromagnetic wave 21-cm line. In the 2020s, 21-cm intensity mapping (IM), which observes the intensity of the 21-cm line, will begin with several large-scale radio interferometers, such as Square Kilomtre Array (SKA). The 21 cm IM can reach a high redshift since it can easily identify the redshift from the observed frequency of emission or absorption line. Observations to the distant universe allow us for more powerful constrain on time-varying dark energy. In addition, by observing the intensity without resolving individual galaxies, 21cm IM can observe a larger region than conventional observations. Since the BAO is a feature on large scales in the power spectrum, the 21-cm IM is expected to provide precise BAO measurements. For example, the 21-cm IM by SKA can explore the large-scale structure as far as redshift $z \sim 3$ (Square Kilometre Array Cosmology Science Working Group et al., 2020). Therefore, it is necessary to develop a theoretical framework for constraining dark energy using BAO in the 21-cm power spectrum of the 21cm line.

However, since the non-linear growth of gravity and complicated astrophysical processes such as UV background radiation and radiations from stars and galaxies affect the time evolution of the HI distribution (Pillepich et al.,

2018a), the HI clustering is not clearly understood. Therefore, although the BAO method based on the 21-cm line will be a powerful tool to constrain dark energy models, non-linear growth of structure and baryon feedback must be modeled in order to achieve a 1% level constraint.

1.4 Aim and structure of this thesis

Since it is difficult to compute the HI power spectrum analytically, several approaches exist to obtain the HI distribution. One is to use cosmological hydrodynamic simulations (Villaescusa-Navarro et al., 2018; Ando et al., 2019). This is relatively close to reality since it includes baryons and dark matter particles and considers the interaction of gravity and baryonic physical processes. However, its computational cost is relatively high, making large-scale calculations difficult. Another is a quasi-analytical model that pastes the HI onto the distribution of dark matter obtained using N-body simulations. This is computationally lesser than cosmological hydrodynamic simulations and allows for the simulation with large box-size such as Gpc scales. This approach is mainly based on the dark matter halo (Wang et al., 2021; Sarkar et al., 2016; Sarkar & Bharadwaj, 2018; Modi et al., 2019). This is based on the result that most HI is present in the high-density region after reionization, as revealed by the Lyman-alpha observations (Wyithe & Loeb, 2008). The other gives the HI density fluctuations depending on the value of the dark matter density fluctuations (Sinigaglia et al., 2021). In addition, there is a method that uses Generative Adversarial Networks (GAN) to create HI distributions from dark matter distributions (Zamudio-Fernandez et al., 2019).

In this thesis, I propose a new and simple method for generating HI distributions that reproduce the shape of the HI power spectrum in preparation for the development of the theoretical framework for the future 21-cm line surveys. Since the BAO analysis uses only the position of the peaks and troughs of the BAO wiggle in the HI power spectrum, the slope of the power spectrum is essential, not the amplitude. Since accurate measurement of BAO signals on the scale of about 100 Mpc requires the simulation with Gpc scales, I use N-body simulation instead of cosmological hydrodynamic simulation. In this thesis, the quasi-analytical method using halos in the previous studies, I propose a new method to generate the HI density field.

This thesis is organized as follows. In chapter 2, I introduce the standard cosmological model. I first that encompasses the accelerating expansion of the Universe and the basis of the BAO. Initially I discuss the growth of the uniform density field as the background component and accelerated expansion. Then, I describe the growth of the density fluctuation, which is the perturbation component, and the BAO. Finally, section 2.5 explains the linear

growth of the matter power spectrum. Chapter 3 first describe the physics of the 21-cm line and the differential brightness temperature. Then I describe the 21-cm line power spectrum. Then, section 3.3 provides a brief introduction to the 21-cm line observations. In chapter 4, I explain my simulation setup and how to generate the density field. I also show the relationship between the location of HI gas and the HI power spectrum in section 4.2. In chapter 5, I propose a method to generate the HI density field and discuss the effectiveness of this method. Furthermore, a comparison with the methods of previous studies is given in section 5.2, a discussion involving density fluctuations is given in section 5.3, the effect of spin-temperature fluctuations on the 21-cm line power spectrum is given in section 5.4, and the results of evaluating the proposed method at different redshifts are summarized in section 5.5. Finally, I summarize this work and discuss future prospects in chapter 6.

Chapter 2

Standard cosmology

This chapter summarizes the basic ideas and equations in cosmology and briefly introduces the Baryon Acoustic Oscillations (BAO) that will be discussed in the following chapters.

2.1 Friedmann Equation

The cosmological principle says that there is no special place and direction in the Universe on large scales. In this section, we first derive the time evolution of the uniform isotropic universe. The Einstein equation is

$$G^{\mu}_{\nu} + \Lambda\delta^{\mu}_{\nu} = 8\pi G T^{\mu}_{\nu}, \tag{2.1}$$

where G^{μ}_{ν} is Einstein tensor and Λ is a cosmological constant. The source term on the right-hand side of the equation, T^{μ}_{ν}, is the energy-momentum tensor. For an ideal fluid that is homogeneous and isotropic, its components are given by

$$T^0_0 = -\rho, \quad T^i_0 = T^0_j = 0, \quad T^i_j = p. \tag{2.2}$$

The FRW metric, which is the metric in the homogeneous and isotropic Universe, is written as

$$ds^2 = -dt^2 + a^2(t)\left[\frac{dr^2}{1-Kr^2} + r^2(d\theta^2 + \sin^2\theta d\phi^2)\right], \tag{2.3}$$

where $a(t)$ is a scale factor of the Universe and K is a spatial curvature. The scale factor is usually normalized as $a(t_0) = 1$ where t_0 is present time. In the following chapters, instead of the scale factor, we sometimes use redshift z, which is defined by

$$1 + z \equiv a^{-1}\,. \tag{2.4}$$

Using the FRW metric, the Einstein tensor can be rewritten by

$$G^0_0 = -3\left[\left(\frac{\dot{a}}{a}\right)^2 + \frac{K^2}{a^2}\right] \tag{2.5}$$

$$G^i_0 = G^0_i = 0. \tag{2.6}$$

$$G^i_j = -\left[2\frac{\ddot{a}}{a} + \left(\frac{\dot{a}}{a}\right)^2 + \frac{K^2}{a^2}\right]\delta^i_j\,. \tag{2.7}$$

Then, substituting Eq. (2.2) and Eq. (2.5) into the Einstein equation yields the following Friedmann equation,

$$\left(\frac{\dot{a}}{a}\right)^2 = \frac{8\pi G}{3}\rho - \frac{K}{a^2} + \frac{\Lambda}{3}\,. \tag{2.8}$$

Similarly, substituting the spatial components Eq. (2.2) and Eq. (2.7) into the Einstein equation yields the acceleration equation,

$$\frac{\ddot{a}}{a} = -\frac{4\pi G}{3}(\rho + 3p) + \frac{\Lambda}{3}\,. \tag{2.9}$$

The above two equations are not independent from the continuity equation of total matter, which is derived from the time component of the conservation laws of the energy-momentum tensor. From $T^{\mu\nu}_{\ ;\nu} = 0$, we obtain

$$\dot{\rho} = -3H(\rho + p)\,, \tag{2.10}$$

where $H \equiv \dot{a}/a$ is the Hubble parameter. It is convenient to introduce the equation of state parameter defined by

$$w \equiv \frac{p}{\rho}\,. \tag{2.11}$$

Then the continuity equation is expressed as

$$\dot{\rho} = -3H(1+w)\rho\,. \tag{2.12}$$

The equation of state parameters are $w = 1/3$ and $w = 0$ for relativistic and non-relativistic matters, respectively, which lead to time evolution of energy densities as $\rho \propto a^{-4}$ and $\rho \propto a^{-3}$ for relativistic and non-relativistic matters, respectively.

2.2 Accelerating Expansion of the Universe

If $\Lambda = 0$, Eq. (2.9) states that normal matter, whose energy density and pressure are both positive, should make the expansion of the universe decelerate ($\ddot{a} < 0$). It is a consequence of the fact that gravity is an universal attractive force. Therefore, matter alone cannot cause accelerated expansion under general relativity. Therefore, to realize the accelerating expansion of the universe, we need to introduce an unknown energy component, called dark energy, whose equation of state parameter $w \equiv p/\rho$ is $w < -1/3$. The cosmological constant Λ has $w = -1$, which is one of the representative models of dark energy, and the ΛCDM model is considered as a standard model. The recent CMB observation (Planck Collaboration et al., 2020) reported $w = -1.028 \pm 0.031$ when assuming that the equation of state of dark energy is time-invariant, which is consistent with a cosmological constant Λ.

2.3 Cosmological Perturbation Theory

While the distribution of matter in our Universe is inhomogeneous and anisotropic, the universe is nearly homogeneous and isotropic on large scales in average. Therefore, it may be possible to develop a perturbation theory, where the Einstein gravitational equation and the fluid equation may be solved by first assuming a homogeneous and isotropic universe as the zeroth order, and then the deviations from the zeroth-order solution are solved as linearized perturbations.

The perturbed FRW metric is written as

$$ds^2 = -a(\tau)^2(1+2\Psi)d\tau^2 + a(\tau)^2(1-2\Phi)\delta_{ij}dx^i dx^j \tag{2.13}$$

where $\Psi(x,\tau)$ and $\Phi(x,\tau)$ are called gravitational potential and curvature perturbation, respectively, and assumed to be small. Here we assumed that the Universe is spatially flat for simplicity. From the metric above, one can calculate the Einstein tensor at linear order as

$$G^0_0 \simeq -\frac{3}{a^2}\mathcal{H}^2 + \frac{2}{a^2}\left[3\mathcal{H}^2\Psi + 3\mathcal{H}\Phi' - \Phi^{,k}_{,k}\right] , \tag{2.14}$$

$$G^0_i \simeq -\frac{2}{a^2}\left[\mathcal{H}\Psi_{,i} + \Phi'_{,i}\right] , \tag{2.15}$$

$$\begin{aligned} G^i_j \simeq & -\frac{1}{a^2}(\mathcal{H}^2 + 2\mathcal{H}')\delta^i_j + \frac{1}{a^2}\left[\Phi^{,i}_{,j} - \Psi^{,i}_{,j}\right. \\ & + \left.\left\{2(\mathcal{H}^2 + 2\mathcal{H}')\Psi + \Psi^{,k}_{,k} - \Phi^{,k}_{,k} + 2\mathcal{H}(2\Phi' + \Psi') + 2\Phi''\right\}\delta^i_j\right] \end{aligned} \tag{2.16}$$

where a dash denotes a derivative with respect to the conformal time τ, and $\mathcal{H} \equiv a'/a$ is the conformal Hubble parameter. For the matter part, we consider

the ideal fluid expression for the energy-momentum tensor that is given by

$$T^{\mu}_{\nu} = p g^{\mu}_{\nu} + (\rho + p) u^{\mu} u_{\nu} \ , \tag{2.17}$$

where p is pressure, ρ is energy density, and u^{μ} is the four-velocity of the fluid. In a perturbed FRW universe with the metric (Eq. (2.13)), the four-velocity is given by

$$u^0 = a^{-1}(1 - \Psi) \ , \tag{2.18}$$
$$u^i = a^{-1} v^i \ , \tag{2.19}$$

where $v^i = dx^i/d\tau$ is the coordinate velocity. The covariant four-velocity is then given as

$$u_0 = -a(1 + \Psi) \ , \tag{2.20}$$
$$u_i = a v_i \ , \tag{2.21}$$

where v_i is defined by $v_i \equiv \delta_{ij} v^j$. Combining the equations above, we find the perturbed energy-momentum tensor as

$$T^0_0 \simeq -\bar{\rho}(\tau) + \delta\rho(\vec{x}, \tau) \ , \tag{2.22}$$
$$T^0_i \simeq -\left(\bar{\rho}(\tau) + \bar{p}(\tau)\right) v_i(\vec{x}, \tau) \ , \tag{2.23}$$
$$T^i_j \simeq \left(\bar{p}(\tau) + \delta p(\vec{x}, \tau)\right) \delta^i_j + \Sigma^i_j(\vec{x}, \tau) \ , \tag{2.24}$$

where the bars denote the homogeneous part of the fluid variables, and we introduced Σ^i_j as an anisotropic pressure perturbation of the fluid that satisfies the traceless condition $\Sigma^i_i = 0$. Using the expressions for G^{μ}_{ν} and T^{μ}_{ν}, we obtain the perturbed Einstein equations in Fourier space as follows

$$k^2\Phi + 3\mathcal{H}(\Phi' + \mathcal{H}\Psi) = -4\pi G a^2 \bar{\rho}\delta \ , \tag{2.25}$$
$$\Phi' + \mathcal{H}\Psi = -4\pi G a^2 (\bar{\rho} + \bar{p}) v \ , \tag{2.26}$$
$$\Phi'' + \mathcal{H}(\Psi' + 2\Phi') + (2\mathcal{H}' + \mathcal{H}^2)\Psi + \frac{k^2}{3}(\Phi - \Psi) = 4\pi G a^2 \delta p \tag{2.27}$$
$$\Phi - \Psi = -8\pi G a^2 \Sigma \ . \tag{2.28}$$

Note that we only considered the scalar part of perturbations and defined scalar velocity and scalar anisotropic stress in Fourier space as

$$v^i(\vec{x}, \tau) = \int \frac{d^3k}{(2\pi)^3} (ik^i) v(k, \tau) e^{i\vec{k}\cdot\vec{x}} \ , \tag{2.29}$$
$$\Sigma^i_j(\vec{x}, \tau) = \int \frac{d^3k}{(2\pi)^3} \left(-k^i k_j + \frac{k^2}{3}\delta^i_j\right) \Sigma(k, \tau) e^{i\vec{k}\cdot\vec{x}} \ . \tag{2.30}$$

For the matter part, the evolution equations of density perturbation $\delta \equiv \delta\rho/\bar{\rho}$ and velocity v can be derived from the conservation of the energy-momentum

tensor, which is a consequence of the Einstein equation. The perturbed part of the conservation of the energy-momentum tensor,

$$T^{\mu}_{\nu;\mu} = \partial_\mu T^\mu_\nu + \Gamma^\alpha_{\alpha\beta} T^\beta_\nu - \Gamma^\beta_{\nu\alpha} T^\alpha_\beta = 0 \,, \tag{2.31}$$

gives the following equations in Fourier space

$$\delta' = (1+w)k^2 v + 3(1+w)\Phi' - 3\mathcal{H}\left(\frac{\delta p}{\delta\rho} - w\right)\delta \,, \tag{2.32}$$

$$v' = -\mathcal{H}(1-3w)v - \frac{w'}{1+w} - \frac{\delta p}{(1+w)\bar{\rho}} + \frac{2k^2}{3(1+w)\bar{\rho}}\Sigma - \Psi \,, \tag{2.33}$$

where $w = \bar{p}/\bar{\rho}$ is the equation of state of the fluid. For a non-relativistic fluid such as baryon and cold dark matter without any interactions, $w = 0$ and $\delta p = \Sigma = 0$, the above equations are reduced to

$$\delta'_m = k^2 v_m + 3\Phi' \,, \tag{2.34}$$

$$v'_m = -\mathcal{H} v_m - \Psi \,, \tag{2.35}$$

where the subscript $m = (c,\ b)$ stands for non-relativistic matter (cold dark matter or baryon). These two equations simply state that the density contrast evolves according to the velocity divergence and the stretching of the three-dimensional space, and the velocity evolves according to the gradient of the gravitational potential with friction due to the Hubble expansion. For a relativistic fluid such as photons and neutrinos, $w = 1/3$ and $\delta p/\delta\rho = 1/3$. In this case, the equations become

$$\delta'_r = \frac{4k^2}{3} v_r + 4\Phi' \,, \tag{2.36}$$

$$v'_r = -\frac{1}{4}\delta_r + \frac{k^2}{6}\Pi_r - \Psi \,, \tag{2.37}$$

where we defined $\Pi \equiv \Sigma/\bar{p}$ as the normalized anisotropic pressure. For relativistic species such as photon and neutrino, the anisotropic pressure is not negligible in the Euler equation. In practice, we should solve the Boltzmann equation to evaluate Π.

These equations are valid only for an uncoupled fluid or for the total matter. However, they should be modified for the components with interactions. An important interaction we need to consider is Thomson scattering, which couples photons and baryons in the primordial plasma before recombination. With the scattering term included, the Euler equations for baryon and photon are modified to

$$v'_b + \mathcal{H} v_b + \Psi = -\frac{4}{3}\frac{\bar{\rho}_\gamma}{\bar{\rho}_b} a n_e \sigma_T (v_b - v_\gamma) \,, \tag{2.38}$$

$$v'_\gamma + \frac{1}{4}\delta_\gamma - \frac{k^2}{6}\Pi_\gamma + \Psi = -a n_e \sigma_T (v_\gamma - v_b) \,, \tag{2.39}$$

where n_e is the number density of free electrons and σ_T is the Thomson scattering cross section. The prefactor in the right hand side of Eq. (2.38), $-(4\bar{\rho}_\gamma/3\bar{\rho}_b)$ comes from the momentum conservation of the total matter (baryon plus photon). When the interaction is frequent, or in other words $an_e\sigma_T/H \gg 1$, baryon and photon tightly couple with each other and move together, $v_\gamma \simeq v_b$.

2.4 Baryon Acoustic Oscillations

In the primordial plasma before recombination, the number density of free electrons was so large that baryons and photons are tightly coupled. The mean free time for a photon to scatter off free electrons is given by $\tau_c = (an_e\sigma_T)^{-1}$, which is a much shorter time scale than the Hubble time scale $\mathcal{H}^{-1}$. The large prefactor $an_e\sigma_T$ on the right hand side of Eqs.(2.38) and (2.39) makes it difficult to solve the equations numerically. Therefore, in this limit, we usually use the tight coupling approximation (TCA) where we expand the perturbation equations assuming that the dimensionless parameters $k/(an_e\sigma_T)$ and $\mathcal{H}/(an_e\sigma_T)$ are small (Peebles & Yu, 1970).

At the zeroth order in TCA where $k/(an_e\sigma_T) \to 0$, we obtain $v_b = v_\gamma$ and $\Pi_\gamma = 0$, namely, the frequent Thomson scattering makes the distribution of photons to be isotropic, and the photons and baryons move together. To obtain the evolution equations valid for the first order TCA, we first combine the continuity equations for baryons and photons to find

$$\delta'_\gamma = \frac{4}{3}k^2 v_\gamma + 4\Phi' \,, \tag{2.40}$$

$$\delta'_b - \frac{3}{4}\delta'_\gamma = k^2(v_b - v_\gamma) \,. \tag{2.41}$$

Putting the zeroth order solution $v_b = v_\gamma$, we find $\delta'_b = \frac{3}{4}\delta'_\gamma$. Therefore, if we put the adiabatic initial condition where $\delta_b = \frac{3}{4}\delta_\gamma$ initially, it holds at later times as long as the tight coupling approximation holds. Next, we combine the Euler equations for baryon and photon to eliminate the prefactor $an_e\sigma_T$. Using again the zeroth order solution $v_b = v_\gamma$ and $\Pi_\gamma = 0$, we find

$$v'_\gamma + Rv'_\gamma + R'v_\gamma + \frac{1}{4}\delta_\gamma + (1+R)\Psi = 0 \,, \tag{2.42}$$

where we define

$$R \equiv \frac{3}{4}\frac{\rho_b}{\rho_\gamma} \,. \tag{2.43}$$

Eliminating v_γ using Eqs. (2.42) and (2.40), we obtain

$$\delta''_\gamma + \frac{R'}{1+R}\delta'_\gamma + \frac{k^2}{3(1+R)}\delta_\gamma = -\frac{4k^2}{3}\Psi + \frac{4R'}{1+R}\Phi' + 4\Phi'' \,. \tag{2.44}$$

This is an equation for an oscillator with gravitational potentials as source terms. Because $R' = \mathcal{H}R$, after the horizon crossing when $k/ > 1$ the second (friction) term can be omitted compared to the third term in the left-hand side of the equation. Moreover, in the radiation dominated era the gravitational potentials Ψ and Φ decay soon after the horizon crossing. Therefore the above equation reduces to

$$\delta_\gamma'' \simeq -\frac{k^2}{3(1+R)}\delta_\gamma \,, \tag{2.45}$$

and we may find the solution

$$\delta_\gamma \simeq A\cos(kr_s) + B\sin(kr_s) \,, \tag{2.46}$$

where A and B are integration constants to be determined from initial conditions. Here we defined the sound horizon of the baryon-photon fluid as

$$r_s(\tau) \equiv \int \frac{d\tau}{\sqrt{3(1+R)}} = \int c_s d\tau \,, \tag{2.47}$$

where we introduced the sound speed of the baryon-photon fluid

$$c_s^2 \equiv \frac{\dot{P}_\gamma + \dot{P}_b}{\dot{\rho}_\gamma + \dot{\rho}_b} = \frac{1}{3}\frac{1}{1+\frac{\dot{\rho}_b}{\dot{\rho}_\gamma}} = \frac{1}{3}\frac{1}{1+R} \,. \tag{2.48}$$

In the tight coupling approximation where $v_b \simeq v_\gamma$ and $\delta_b \simeq \frac{3}{4}\delta_\gamma$, the photon and baryon fluids move together and undergo the acoustic oscillations given by Eq. (2.46), which is called the Baryon Acoustic Oscillations (BAO). The oscillations are driven by the pressure mainly due to photons in the radiation dominated era where $R \ll 1$ and around the epoch of recombination where $R \sim \mathcal{O}(1)$. After recombination, these oscillations gravitationally imprint the wiggles in the matter power spectrum, as shown in Fig. (2.1). Fig 2.2 shows the growth of the density fluctuation of the matter and baryon, and we see that the acoustic oscillations of baryons and then catching up to the dark matter fluctuations.

2.5 Matter Power spectrum

In this section, we introduce the linear growth of the matter fluctuation and the matter power spectrum. In the radiation dominant era, the fluctuations below the horizon scale cannot grow due to radiation pressure. From Eq. (2.25), Eq. (2.36), and Eq. (2.37), the growth of the density fluctuation in the matter dominant era is described by

$$\ddot{\delta} + H\dot{\delta} - 4\pi G\bar{\rho}a^2\delta = 0 \,. \tag{2.49}$$

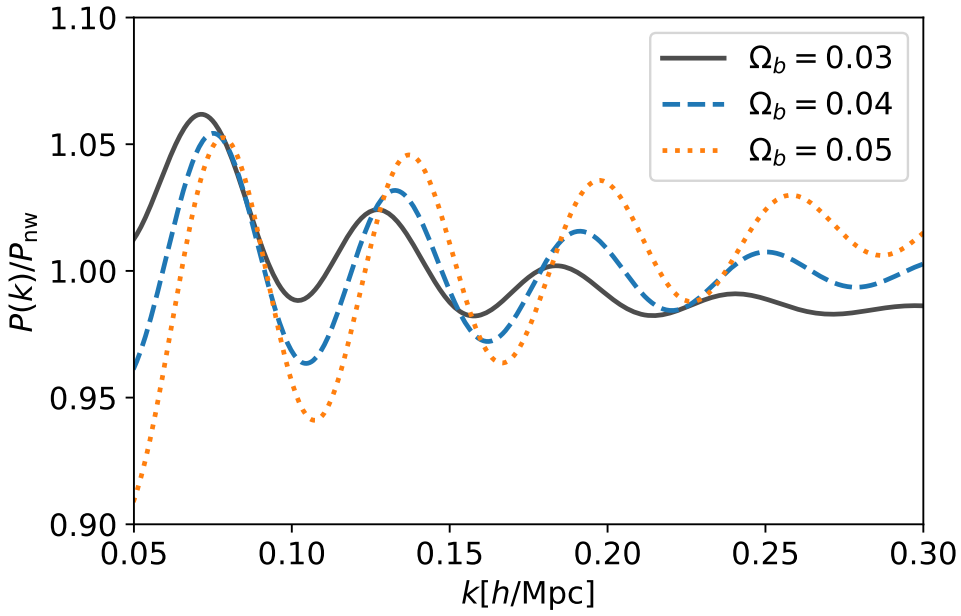

Figure 2.1: BAO wiggle in the matter power spectrum with varying Ω_b as indicated in the figure. The vertical axis is the matter power spectrum divided by the power spectrum without BAO wiggle. As the baryon density parameter increases, the BAO wiggles amplify and shift toward smaller scales because the scale of the sound horizon becomes small.

Solving this differential equation yields

$$D_+ \propto H \int_0^a \frac{da}{d^3 H^3} , \qquad D_- \propto H , \tag{2.50}$$

where D_+ is the growing mode and D_- is the decaying mode, and we neglect the latter. Since the Hubble parameter $H(z)$ is

$$H(z) = H_0 \sqrt{\frac{\Omega_{m0}}{a^3} + \frac{\Omega_{K0}}{a^2} + \Omega_\Lambda} , \tag{2.51}$$

D_+ is called a growth factor that grows in proportion to the scale factor $a(t)$ in the matter dominated era. In linear theory, the matter density contrast can be expressed as

$$\delta_{\rm L}(\boldsymbol{k}, t) = \frac{D(t)}{D(t_{\rm in})} T(k) \delta_{\rm in}(\boldsymbol{k}) , \tag{2.52}$$

where $\delta_{\rm L}(\boldsymbol{k}, t)$ is the linear matter density contrast, $\delta_{\rm in}(\boldsymbol{k})$ is the density contrast at initial time, and $T(k)$ is called the linear transfer function. Due to suppression of growth of matter fluctuations in the radiation-dominated era, the fluctuations below the horizon scale at the matter-radiation equality epoch become small. In the matter dominated era, the evolution of density contrast does not depend on $\boldsymbol{k}$ and expressed by an overall factor $D(t)$ (see Eq. (2.49)). Therefore, the time evolution of the fluctuation from the initial condition can be written in Eq. (2.52) by introducing the transfer function $T(k)$. While transfer function approaches unity in the super-horizon scales, it approaches proportionality of k^{-2} on small scales.

The power spectrum $P(k)$ is the correlation function in the Fourier space, which is defined by

$$\langle \delta(\boldsymbol{k}) \delta(\boldsymbol{k}') \rangle = (2\pi)^3 \delta_{\rm D}(\boldsymbol{k} + \boldsymbol{k}') P(k). \tag{2.53}$$

where $\delta_{\rm D}$ is a 3-dimensional delta function. Substituting Eq. (2.52) into this equation, we obtain the linear power spectrum as

$$P_{\rm L}(k) = \frac{D^2(t)}{D^2(t_{\rm in})} T^2(k) \, P_{\rm in}(k). \tag{2.54}$$

where we defined the initial power spectrum by

$$\langle \delta_{\rm in}(\boldsymbol{k}) \delta_{\rm in}(\boldsymbol{k}') \rangle = (2\pi)^3 \delta_{\rm D}(\boldsymbol{k} + \boldsymbol{k}') P_{\rm in}(k). \tag{2.55}$$

Assuming that the initial power spectrum follows a power law, we have

$$P_{\rm in} \propto k^{n_s}, \tag{2.56}$$

where n_s is the spectral index for the initial power spectrum. The Harrison-Zel'dovich spectrum with $n_s = 1$ is considered to be close to reality, and the CMB observations give a constraint of $n_s = 0.9665 \pm 0.038$ (Planck Collaboration et al., 2020). Fig. (2.3) shows the linear matter power spectrum $P_L(k)$ for some Ω_b values.

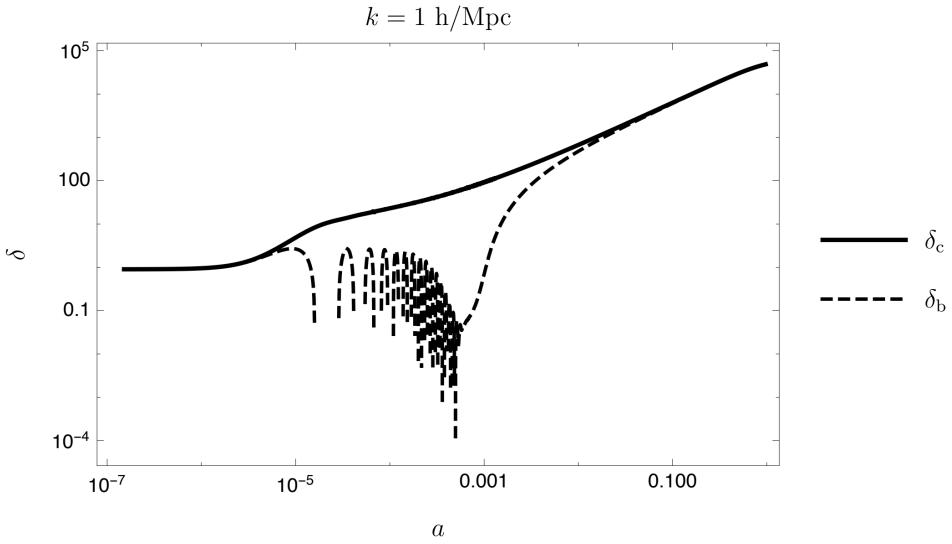

Figure 2.2: The time evolution of the density fluctuations of CDM (solid line) and baryon (dashed line) at $k = 1h\mathrm{Mpc}^{-1}$. After the horizon crossing when $a \gtrsim 10^{-4}$, the baryon density fluctuation undergoes acoustic oscillations while that of CDM gradually evolves by self-gravity. After recombination when $a \gtrsim 10^{-3}$, baryon decoupled from photons and fell into the gravitational potential well due to CDM so that the baryon density fluctuation δ_b catched up the CDM density fluctuation δ_c. This figure is adopted from arxiv:1803.00070 (Piattella, 2018).

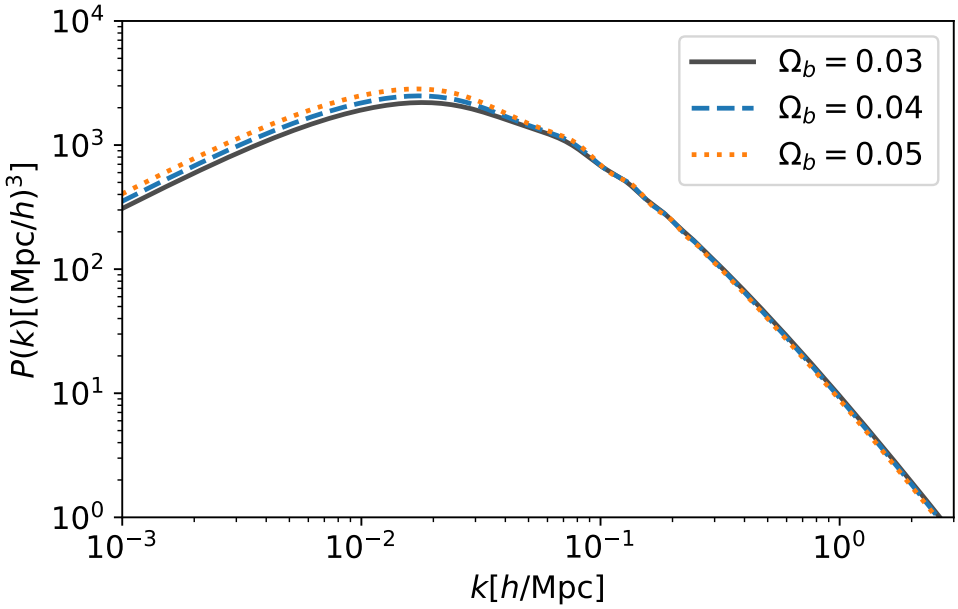

Figure 2.3: The linear matter power spectrum with varying the value of $\Omega_b = 0.03$, 0.04, and 0.05. The peak at $k \simeq 10^{-2}$ [Mpc/h] corresponds to the horizon scale at matter-radiation equality, and the suppression on smaller scales is due to the fact that the matter fluctuations could not grow when the universe was radiation dominated.

Chapter 3

The 21-cm signal at the epoch of post-reionization

21-cm IM mapping explores the large-scale structures by measuring the differential brightness temperature. This chapter introduces the differential brightness temperature of the 21-cm line at the epoch of post-reionization. Then, we describe the 21-cm line power spectrum.

3.1 Differential brightness temperature

The 21-cm line is observed by the differential brightness temperature, which is described by the difference between the spin temperature of the HI cloud and the temperature of the background radio loud source.

$$\delta T_{\rm b} = \frac{T_{\rm S} - T_\gamma(z)}{1+z}\left(1 - e^{-\tau_{\nu_0}}\right), \tag{3.1}$$

where $T_{\rm S}$ is the spin temperature. T_γ is the temperature of background source and we use CMB temperature for the 21-cm IM. τ_{ν_0} is a optical depth of the 21-cm line. When the spin temperature is higher than the CMB temperature, the 21-cm line is observed as an emission line, and vice versa as an absorption line. The 21-cm line is emitted due to the spin-flip of a proton and an electron of the hydrogen, and the spin temperature describes the number of states of its hyperfine structure,

$$\frac{n_1}{n_0} = 3\exp\left[-\frac{h\nu_0}{k_{\rm B}T_{\rm S}}\right] \tag{3.2}$$

where n_1 and n_0 is the number of the excited and ground state respectively, and $\nu_0 \sim 1420$MHz is the rest-frame frequency of the 21-cm line. The spin temperature is coupled to the gas kinetic temperature $T_{\rm K}$, the CMB temperature T_γ, and the Lyα color temperature T_α and is described using the coupling

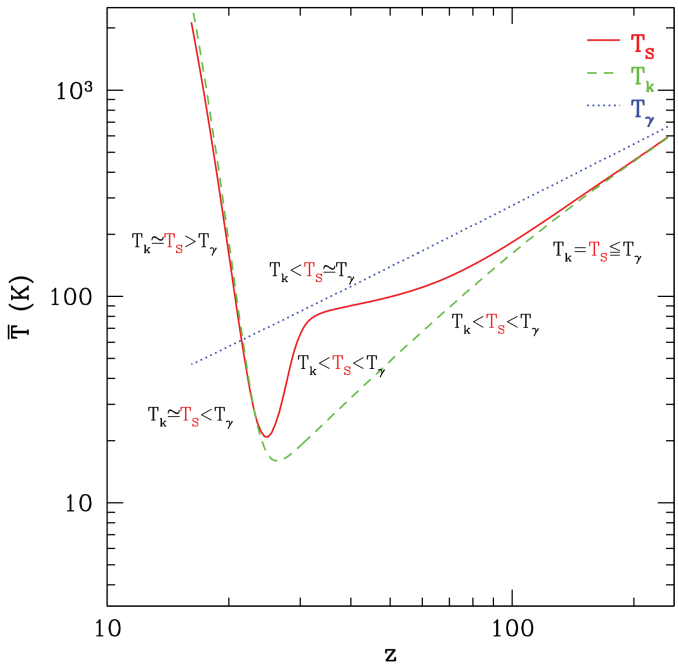

Figure 3.1: The thermal history. Shown are spin temperature (red solid line), gas kinetic temperature (green dashedline), and CMB temperature (blue dotted line). This figure is adopted from Mesinger et al. (2011).

coefficients as follows

$$T_{\rm S}^{-1} = \frac{T_\gamma^{-1} + x_\alpha T_\alpha^{-1} + x_c T_{\rm K}^{-1}}{1 + x_\alpha + x_c}, \tag{3.3}$$

where x_c and x_α are the coupling coefficients of $T_{\rm K}$ and T_α, respectively. Since the Lyα color temperature is coupled to the gas temperature due to atomic recoil, $T_\alpha \sim T_{\rm K}$. Fig 3.6 shows the redshift evolution of the spin temperature. Depending on the redshift, whether the spin temperature is coupling to the gas temperature or the CMB temperature varies.

The optical depth of the 21-cm is described by

$$\tau_{\nu_0} = \frac{3}{32\pi} \frac{hc^3 A_{10}}{k_{\rm B} T_{\rm S} \nu_0^2} \frac{n_{\rm HI}}{(1+z)(dv_\parallel/dr_\parallel)}, \tag{3.4}$$

where $A_{10} = 2.85 \times 10^{-15} s^{-1}$ is the Einstein A coefficient, $dv_\parallel/dr_\parallel$ is the derivative of the velocity along the line of sight, and $n_{\rm HI}$ is the number density of the HI. From Eq 3.1 and Eq 3.4, the differential brightness temperature is rewritten by

$$\delta T_b \approx \frac{3}{32\pi} \frac{hc^3 A_{10}}{k_{\rm B} \nu_0^2} \left(1 - \frac{T_\gamma(z)}{T_{\rm S}}\right) \frac{n_{\rm HI}}{(1+z)H(z)}. \tag{3.5}$$

In the early Universe, since gas temperature is coupled to the CMB temperature through the Compton scattering, there is no 21-cm signal. At $z \leq 100$, according to $T_\gamma \propto (1+z)$ and $T_{\rm K} \propto (1+z)^2$, the CMB temperature is higher than gas temperature. Since spin temperature is coupled to the gas temperature by the collision, the $T_{\rm S} = T_{\rm K} < T_\gamma$ and the 21-cm signal becomes absorption. After that, the gas density decreases due to the expansion of the Universe, and the coupling with the gas is broken, and the spin temperature approaches the CMB temperature. At $25 \leq z \leq 35$, the first stars and galaxies are formed, and they emit X-rays and Lyα photons. The Lyα photons cause coupling between the spin temperature and the gas temperature, and we call it the Wouthuysen-Field (WF) effect (Wouthuysen, 1952). At the same time, these high-energy photons heat the gas, so the 21-cm is observed as an emission line. At $7 \leq z \leq 16$, since the gas temperature is sufficiently high compared to the CMB temperature and thus $T_\gamma/T_{\rm S}$ becomes zero, the 21-cm signal doesn't depend on the temperature. After reionization, since most hydrogen is ionized and the HI remains only in high density regions such as the halo. Therefore the spatial mean of the differential brightness temperature is zero and the spatial distribution of the 21-cm signal can be used to probe the large-scale structures.

3.2 The 21-cm power spectrum

Our goal is the cosmological analysis using BAO wiggles in the power spectrum measured by the 21-cm IM. In Sec 2.5, I discussed the theoretical prediction of the matter power spectrum, and in this section I present the 21-cm line power spectrum. Since we can neglect the effect of the fluctuations of the spin temperature at the post-reionization epoch, the spatial fluctuation of the differential brightness temperature only depends on the HI density fluctuation. Therefore the power spectrum of the differential brightness temperature is proportional to the HI power spectrum.

$$P_{\delta T_b}(k) \propto P_{\rm HI}(k). \tag{3.6}$$

Since the BAO analysis only uses the peak location of the BAO wiggles, it require the shape of the power spectrum and the amplitude does not matter. In this thesis, I basically use the HI power spectrum for the analysis, and I quantitatively show the effect of spin-temperature fluctuations in Sec 5.4.

The growth of the HI density field is strongly affected by the UV background radiation, star-formation, supernova explosions, active galactic nuclei (AGN) feedback, etc., and is therefore difficult to calculate analytically. Previous studies measured the scale-dependent HI bias by using cosmological hydrodynamic simulations (Villaescusa-Navarro et al., 2018; Ando et al.,

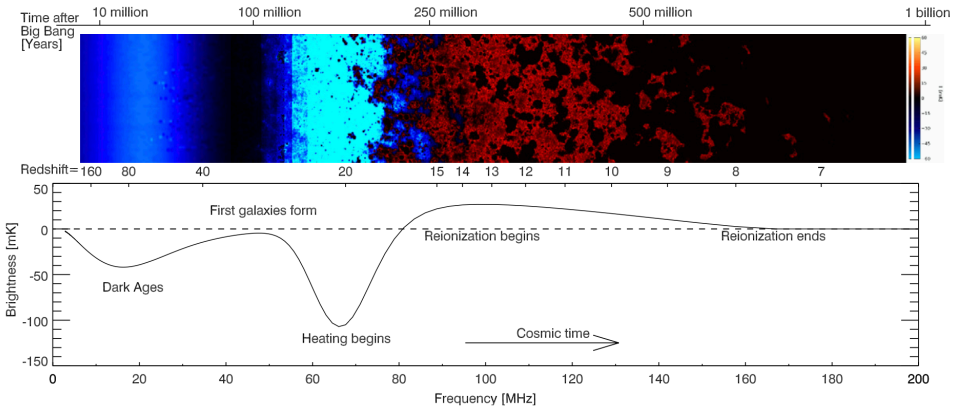

Figure 3.2: The global thermal history of the IGM. Upper panel: the color represents the intensity of the differential brightness temperature and its spatial distribution. Bottom panel: the spatial mean of the differential brightness temperature. This figure is adopted from Pritchard & Loeb (2012).

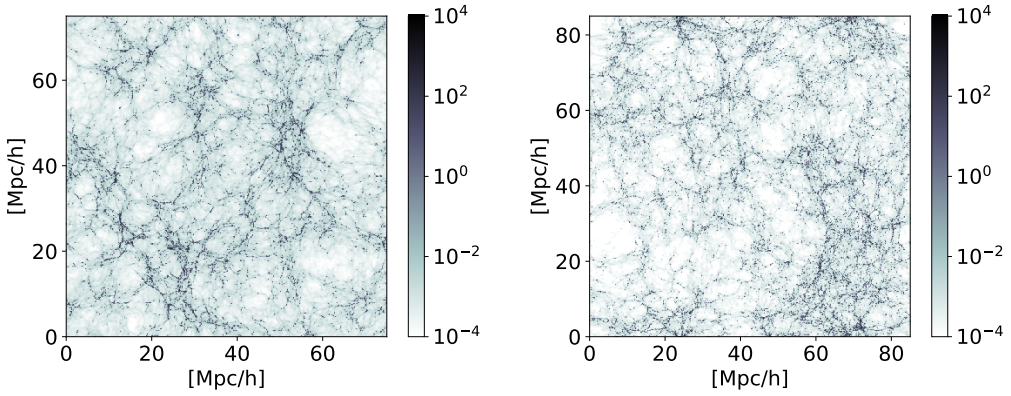

Figure 3.3: HI density map at $z = 3$ calculated from the Illustris-3 simulation (left) and the GADGET3-Osaka simulation (right). Color gradient represents the value of the HI density fluctuation $1 + \delta = \rho_{\rm HI}/\bar{\rho}_{\rm HI}$.

2019). Ando et al. (2019) used two cosmological hydrodynamic simulations to measure the scale dependence of the HI bias and show the effect of different baryon feedback models. The calculations were carried out using data from the prior version of IllustrisTNG, Illustris simulation (Nelson et al., 2015), and GADGET3-Osaka (Aoyama et al., 2018; Shimizu et al., 2019). Fig. 3.3 show the HI density contrast at $z = 3$ for each simulation. Fig 3.4 shows the HI bias. While the HI bias asymptotically approaches a constant on the large scales, and has a different scale dependence in two simulations on small scales.

Other than the Illustris and the GADGET3-Osaka simulation, there are cosmological hydrodynamic simulations such as EAGLE (Schaye et al., 2015) and HorizonAGN (Dubois et al., 2016). Figure 3.5 shows the box size and resolution of current cosmological hydrodynamic simulations. High computational cost makes performing the simulation with high-resolution and Gpc scales calculations difficult.

Therefore, Sarkar et al. (2016); Sarkar & Bharadwaj (2018); Wang et al. (2021); Modi et al. (2019) use a method to create the HI density field by pasting the HI onto dark matter halos in the N-body simulation, which takes relatively low computational cost (hereinafter called as pasting method). Sarkar et al. (2016) also shows the scale dependence of the HI bias close to Ando et al. (2019).

3.3 Current observations and future challenges

The absorption feature of the 21-cm global signal was first detected by EDGES (Bowman et al., 2018), but the absorption is deeper than the value predicted by

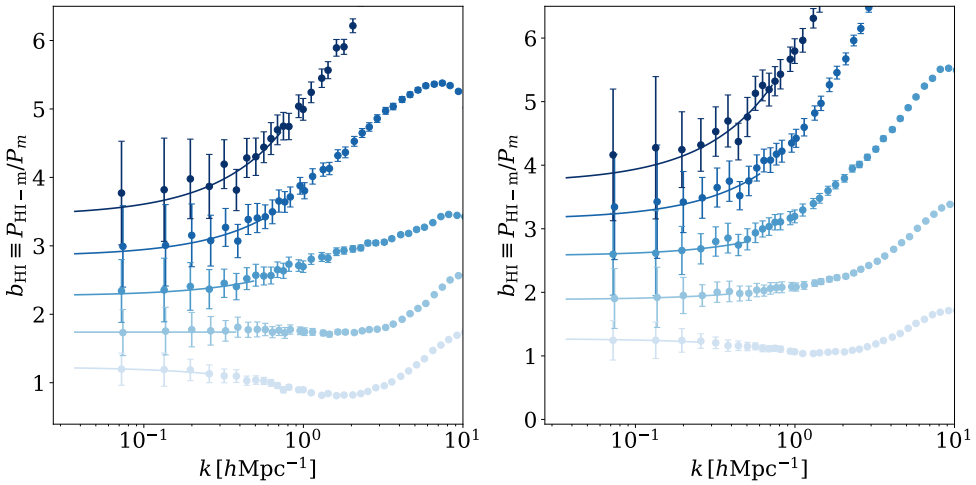

Figure 3.4: HI bias measured from the Illustris-3 simulation (left) and the GADGET3-Osaka simulation (right). In both panels, data points correspond to the bias measured at $z = 5, 4, 3, 2$, and 1 from top (dark blue) to bottom (light blue), respectively. Solid lines are best-fit models where each bias is fitted by a linear function of k. This figure is adopted from Ando et al. (2019).

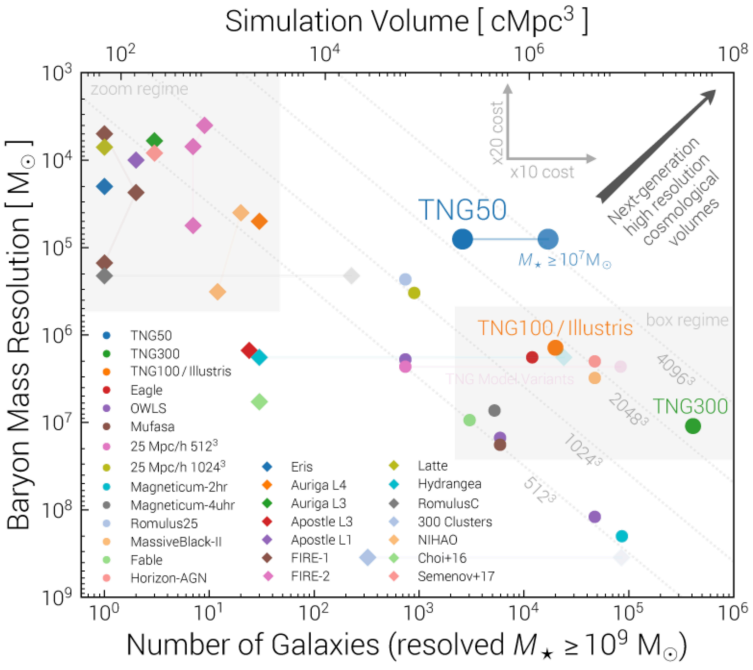

Figure 3.5: The box-size and the resolution of the current cosmological hydrodynamic simulations. This figure is adopted from "project description" in the website of the IllustrisTNG simulation (https://www.tng-project.org/about/).

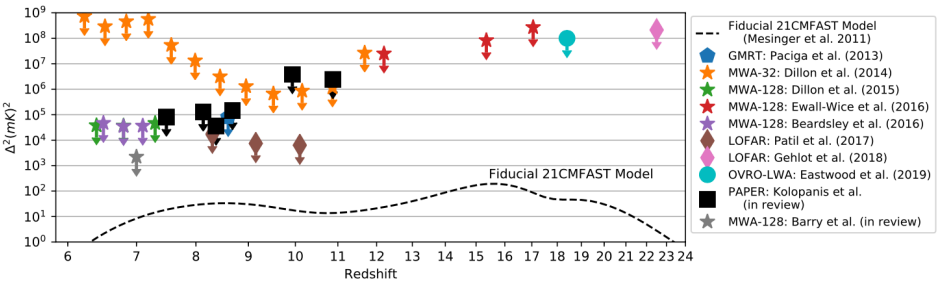

Figure 3.6: Upper limits of the power spectrum given by current 21-cm line experiments. The power spectrum given by the dashed line is a typical theoretical expectation that is calculated using the 21cmFAST code. This figure is adopted from Parsons et al. (2019).

the standard cosmological model. Some experiments have also begun to measure the 21-cm line power spectrum at the epoch of the reionization. Fig 3.6 shows the upper limit on the power spectrum at $k \sim 0.1h\mathrm{Mpc}^{-1}$ by GMRT, HERA, LOFAR, and MWA. Since, they are much larger than the standard model predicted by 21CMFAST (Mesinger et al., 2011), it is expected to be detected by future surveys such as SKA.

The 21-cm IM at the post-reionization is used for the large-scale structure. The 21-cm line after the reionization period is used as a good tracer for the large-scale structure. The frequency of the 21cm line emitted from the HI cloud at redshift z_{obs} is $1.4/(1 + z_{\mathrm{obs}})$ GHz. Therefore, it is easier to identify the redshift from the observed frequency. Figure (3.7) shows the survey volume and the redshift range for the galaxy redshift surveys and 21-cm IM. We see that the intensity mapping by SKA phase-1 will observe a wide area, which means it can measure the power spectrum at BAO scales accurately.

The 21-cm IM at the epoch of post-reionization has already done. (Chang et al., 2010) measure the the 21-cm line at $z \sim 0.8$ with Green Bank Telescope (GBT). Fig 3.8 shows the cross power spectrum between 21-cm intensity by GBT and the WiggleZ galaxies. Anderson et al. (2018) also measured the cross power spectrum between the 21-cm IM by the Parkes 21-cm Multibeam Receiver and galaxy surveys. A serious problem with the 21-cm line survey is the foreground radiation of the Milky Way, which has a intensity about three orders of magnitude higher than the 21-cm line signal from the HI cloud. Correlating with other tracers is used to reduce the effect of foreground emission. However, Tanaka et al. (2018), which correlates with the CMB observation, shows that foreground removal is still an important issue even with cross-correlation. There have been several studies on foreground removal (Switzer

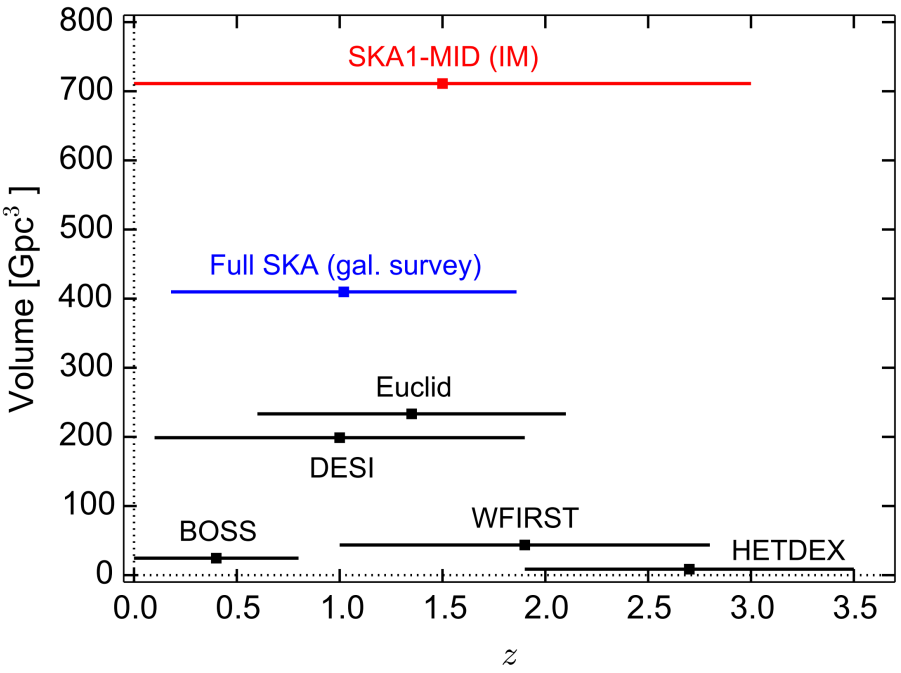

Figure 3.7: Observation volume and redshift range of the galaxy surveys (Euclid, DESI, BOSS WFIRST, HETDEX, Full SKA) and the 21-cm IMs (SKA1-MID) that are scheduled in the near future. This figure is adopted from Santos et al. (2015).

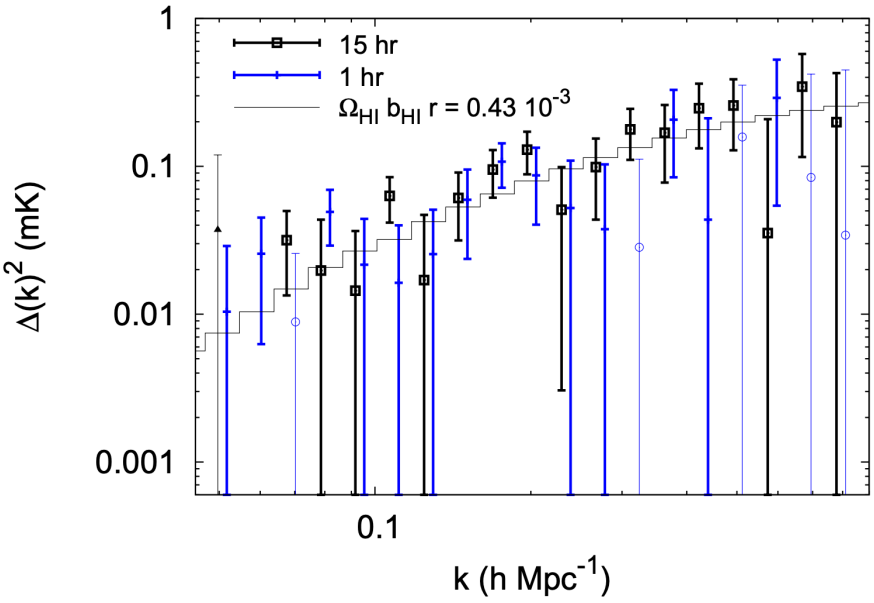

Figure 3.8: Cross-power spectrum between the 21-cm IM by GBT (Chang et al., 2010) and optical galaxies by WiggleZ Dark Energy Surveys (Drinkwater et al., 2010) at $z \sim 0.8$. Thin lines actually take negative values. This figure is adopted from Masui et al. (2013).

et al., 2015; Wolz et al., 2017; Makinen et al., 2021). In this thesis, I ignore the foreground radiation and focus on reproducing the HI distribution in real space.

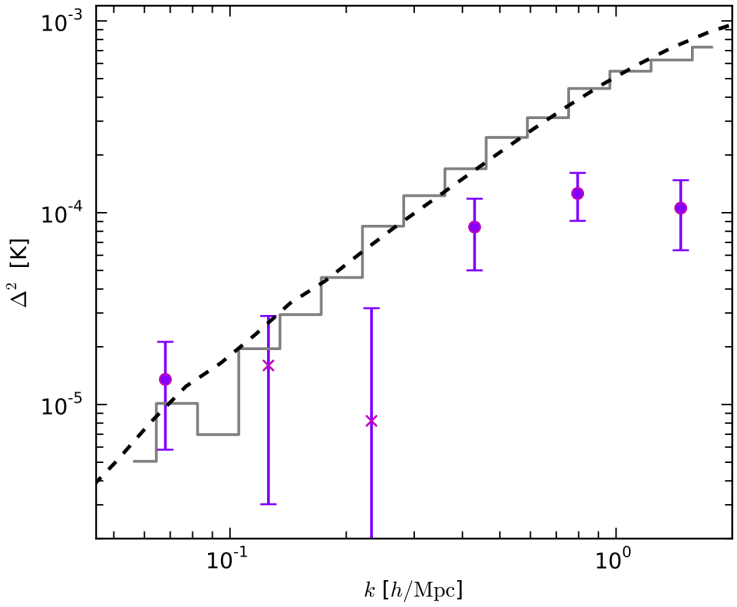

Figure 3.9: 1D Cross power between the 21-cm IM by Parkes (Staveley-Smith et al., 1996) and 2dF galaxies (Colless, 1999) at $z \sim 0.08$. Circles mean positive, and Cross symbols mean the negative value. This figure is adopted from Anderson et al. (2018).

Chapter 4

HI density field from cosmological hydrodynamic simulation

In this chapter, I explore the nature of the HI clustering at redshift $z \leq 3$ in real space. I use the cosmological hydrodynamic simulation, IllustrisTNG simulation (Marinacci et al., 2018; Naiman et al., 2018; Nelson et al., 2018; Pillepich et al., 2018b; Springel et al., 2018; Nelson et al., 2019) to compute the density fluctuations of the HI.

4.1 Cosmological hydrodynamic simulation

4.1.1 IllustrisTNG simulation

IllustrisTNG simulation is a publicly available data of the cosmological magnetohydrodynamical simulation. It solves magnetohydrodynamics using moving-mesh code AREPO (Springel, 2010). The IllustrisTNG is based on the original Illustris simulation (Nelson et al., 2015; Vogelsberger et al., 2014a,b; Genel et al., 2014; Sijacki et al., 2015). The IllustrisTNG employs Planck2015 cosmological parameters (Planck Collaboration et al., 2016). TNG100 and TNG300 simulations have box size of $75h^{-1}\mathrm{Mpc}$ and $205h^{-1}\mathrm{Mpc}$ on a side, respectively. Each realization has three different mass resolutions. It has been shown that the HI power spectrum is highly deformed by the lack of mass resolution of the simulation (Ando et al., 2019). This is simply explained by that the HI mainly resides in the halo, and if we have a low mass resolution, smaller halos do not form in the simulation. Then the HI bias becomes higher than the one from higher-resolution simulations. In order to build a method for reconstructing the HI map that reproduces the realistic HI power spectrum, I use TNG100-1, which has the highest resolution with 2×1820^3 dark-matter (DM) particles and gaseous cells. The mass resolution is $5.1 \times 10^6 h^{-1}\mathrm{M}_\odot$ for dark matter particle and $9.4 \times 10^5 h^{-1}\mathrm{M}_\odot$ for the gaseous cell. The minimum

value of the gravitational softening in comoving units is $\epsilon_{\rm DM,min} = 0.5h^{-1}\,{\rm kpc}$ for dark matter particles and $\epsilon_{\rm gas,min} = 0.125h^{-1}\,{\rm kpc}$ for gas. In addition, in Chapter 5, TNG100-1-Dark, an N-body simulation based on the same initial conditions as TNG100-1, is also used to create the dark matter distribution. The ionization rate of hydrogen is calculated on-the-fly and both photo-ionization and collisional-ionization are taken into account. The spatially uniform and redshift-dependent UV background (UVB) radiation (Faucher-Giguère et al., 2009) is adopted at $z \leq 6$ and self-shielding correction is included in the simulation. A part of the gas particles can be transformed into stars or black holes (BH), and the energy released from the supernova and super-massive black hole are considered. Depending on the mass accretion rate of the gas into the AGN, two types of AGN feedback mode occur (Pillepich et al., 2018a). The quasar mode occurs when the accretion rate is high and has the effect of transporting heat, while the radio mode happens when the accretion rate is low and generates wind from the AGN. There are some updates of the IllustrisTNG simulation from the Illustris simulation. There are some updates, but the most notable one are the modifications of AGN feedback from bubble model to kinetic wind. This modification improves the discrepancy between the Illustris and the observations, such as the galaxy stellar mass function on the massive side. The introduction of magnetic fields also increases the overall HI fraction, in particular at the halo region. Second, the magnetic field is introduced, and this affects the massive halo and suppress the star formation.

Since most HI is located in high-density regions such as halos, I use halos in the analysis of this thesis. The halos in IllustrisTNG have been identified using the Friend-of-Friends (FoF) algorithm with a linking length parameter $b = 0.2$. I use the R_{200c} (`Group_R_Crit200`, the radius where the mean density inside is 200 times the critical density) and M_h (`GroupMass`, sum of all particles in each halo) to define the virial radius and mass of halo, and I assign the halo at position of minimum gravitational potential, `GroupPos`. Other papers used the centre of mass, `GroupCM`, as the definition of halo position. We note that `GroupPos` and `GroupCM` differ significantly; For some halos, the offset between them is comparable or even larger than the virial radius. It is not obvious which halo centre is better to use; however, we see that the HI is more concentrated around the `GroupPos` and I take this as the centre of the halo in this thesis.

4.1.2 Generating density field from particles

As shown later in this section, the sources of inhomogeneity arise from gas density and neutral fraction fluctuations and the spatial variation of spin temperature of the HI, where the latter is often ignored at the epoch of post reion-

ization in the literature. I discussed the HI clustering in real space at $z = 3$, and the HI power spectrum in redshift space is discussed in Villaescusa-Navarro et al. (2018). In order to compute the spatial fluctuation of the density and the power spectrum, it is more convenient to convert the particle data into the density field on the grid. I used the Nearest Grid Point (NGP) method to calculate the density field from the positions and masses of the particles. The NGP method gives whole the masses of the particles to the nearest grid point of the particle, and the density ρ on the grid comes from the total masses of all the contributing particles. The fluid element in the IllustrisTNG simulation occupies a voronoi tessellation cell. However, the size of the voronoi cell is negligibly small compared to my grid size if I take $N_{\rm grid} = 1024^3$, and thus we can treat gaseous cells as point-like object just like the dark matter particles. While all DM particles have equal mass, gas particles have different masses $m_{\rm gas}$ and neutralities x_n. The HI mass in the gas particles is $m_{\rm HI} = m_{\rm gas}\, x_n\, X_H$. The X_H is the fraction of hydrogen in the gas, and I assumed it to be the constant value 0.24 in this thesis. The spatial fluctuation of the density for the tracer α is calculated with the mean density, $\delta_\alpha = \rho_\alpha/\bar{\rho}_\alpha - 1$.

The value of the auto power spectrum is calculated using the density field $\delta_\alpha(\boldsymbol{k})$ in Fourier space as follows

$$P_\alpha(k_i) = \frac{1}{N_{k_i}} \sum_{\{j;k_j \in k_i\}} \delta_\alpha(\boldsymbol{k}_j)\delta^*_\alpha(\boldsymbol{k}_j), \tag{4.1}$$

where wavenumber $\boldsymbol{k}$ has a discrete value and i, j, k is its index and N_k is the number of the modes contained in the k bins. The error bars in the power spectrum were estimated by the approximation (Bernardeau et al., 2002).

$$\sigma^2\left(P_\alpha(k_i)\right) \approx \frac{2P^2_\alpha(k_i)}{N_{k_i}}. \tag{4.2}$$

This approximation is valid on large scales, and I used it in this analysis since I am interested in the power spectrum on large scales $k \leq 1h\mathrm{Mpc}^{-1}$.

4.1.3 The star-forming gas correction

In this thesis, I used the output of IllustrisTNG as the neutral fraction of the gas particles to calculate the HI density. The temperatures of the star-forming gas in the IllustrisTNG simulation are calculated based on Springel & Hernquist (2003), which employs a multiphase model for the star-formation and computes the temperature of the gas particles as a mass-weighted mean of the hot and cold components. However, Villaescusa-Navarro et al. (2018) points out that the neutral rate calculated using that gas temperature, which is the output of the IllustrisTNG simulation, underestimates the HI density compared

to the damped Lyman-α observations (Rao et al., 2006; Lah et al., 2007; Noterdaeme et al., 2012; Songaila & Cowie, 2010; Crighton et al., 2015). Therefore, they recompute the neutral fraction by reducing the gas temperature as a post-process (hereinafter called "the star-forming gas correction").

The star-forming gas correction is consists of two steps. First, Villaescusa-Navarro et al. (2018) fixes the temperature of the star-forming gas particles whose star-formation rate has non-zero value, as $T = 10^4$K and solves the ionization equilibrium to recompute the neutral fraction (Rahmati et al., 2013). The ionization equilibrium is described by

$$n_{\rm HI}(\Gamma_{\rm photo} + \Gamma_{\rm col}) = \alpha_A \, n_{\rm e} \, n_{\rm H_{II}} \tag{4.3}$$

where $\Gamma_{\rm photo}$ is the photoionization rate and $\Gamma_{\rm col}$ is the collisional ionization rate. $n_{\rm HI}$, $n_{\rm e}$, and $n_{\rm H_{II}}$ are the number density of the HI, free electrons and protons, respectively. $\alpha_{\rm A}$ is the recombination rate and Rahmati et al. (2013) describes using the fitting function in Hui & Gnedin (1997) as follows,

$$\alpha_{\rm A} = 1.269 \times 10^{-13} \frac{(315614/T)^{1.503}}{(1 + (315614/0.522T)^{0.47})^{1.923}} \, {\rm cm}^3 \, {\rm s}^{-1}. \tag{4.4}$$

The star-forming gas correction increases the recombination rate and neutral fraction by decreasing the gas temperature T. This greatly increases the HI mass of the star-forming region, especially for the massive halos. This can be separated into two distinct effects; the intrinsic increase of the UV photon, and the effect of self-shielding. Villaescusa-Navarro et al. (2018) also takes the molecular hydrogen component of the gas particles into account using Krumholz, McKee, & Tumlinson model (Krumholz et al., 2008, 2009; McKee & Krumholz, 2010). This slightly decreases the HI mass, and thus in total, the star-forming gas correction works to increase the HI mass. The star-forming gas correction is effective around the halo center, and its effect on the density profile is discussed in section 5.3.

In this chapter, I treat the HI without the correction as fiducial, but in chapter 5, I perform analysis for both cases with and without the star-forming gas correction.

4.2 Where HI resides

In order to create a HI map from the dark matter distribution, we need to know where the HI is located at the epoch of post-reionization. Therefore, I investigate the relationship between the power spectrum and the spatial distribution of the HI using the cosmological hydrodynamic simulation, TNG100-1. The pasting method creates the HI map by giving the HI mass to the center of the halo. However, it is unclear whether the power spectrum can be described

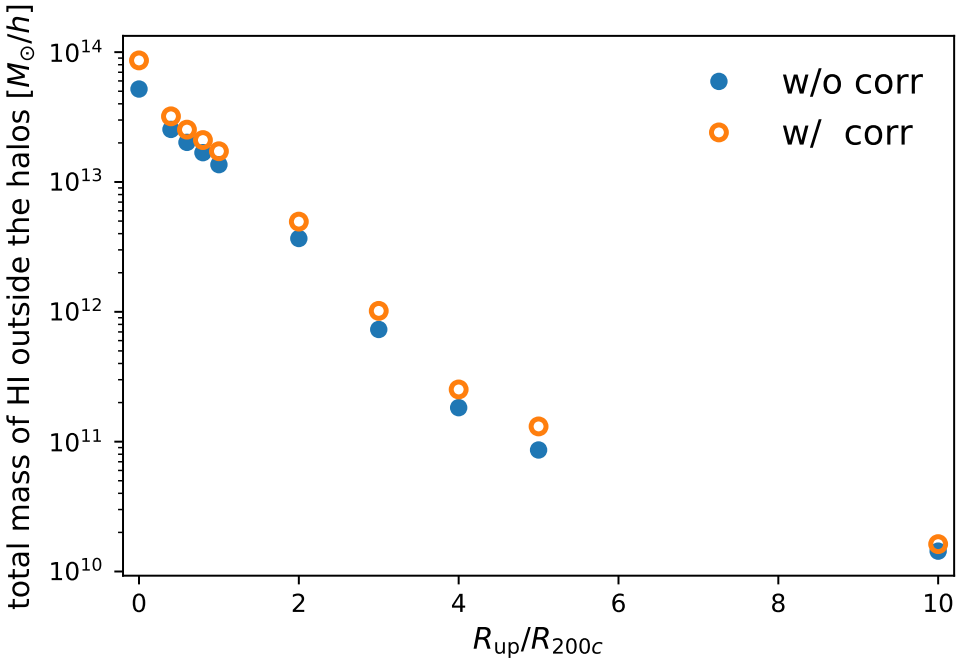

Figure 4.1: Total HI mass outside the radius from the centre of the halo as a function of the ratio $R_{\rm up}/R_{200c}$. The value at $R_{\rm up}/R_{200c} = 0$ is equivalent to the total HI mass in the simulation box. Blue open circle is the case without the star-forming gas correction, and orange circle is that with the star-forming gas correction.

only by the HI in the halo. We first measure the HI mass outside a sphere of constant radius from the center of the halo. We call this sphere "spherical over-density (SO) region" in this thesis and the radius distance SO radius $R_{\rm up}$. Fig 4.1 shows the total HI mass at outside region of the sphere for different SO radii. For the case without the star-forming gas correction, we find that 26% of the total HI mass in the simulation box is outside the sphere of the halo radius $R_{\rm up} = R_{\rm 200c}$. In contrast, 84% of the total mass of dark matter resides outside the halo. These indicate that HI is more localized in the halo than dark matter, but that the mass outside the halo is not negligible.

Next, we compare the power spectrum using only the HI inside the halo for different $R_{\rm up}$ to see how much the HI within and around the halo contributes to the total HI power spectrum. At first, we create the density field (hereinafter called HI,so density field) using only gas particles inside the sphere at constant times the halo radius as shown in Fig 4.2. Then I compute the HI,so power spectrum from it. Figure 4.3 compares the HI power spectra for different radii, $R_{\rm up} = 0.6, 1, 2$, and 3, and the HI power spectrum using all gas particles. The goal is to determine the peak and trough scales of the BAO

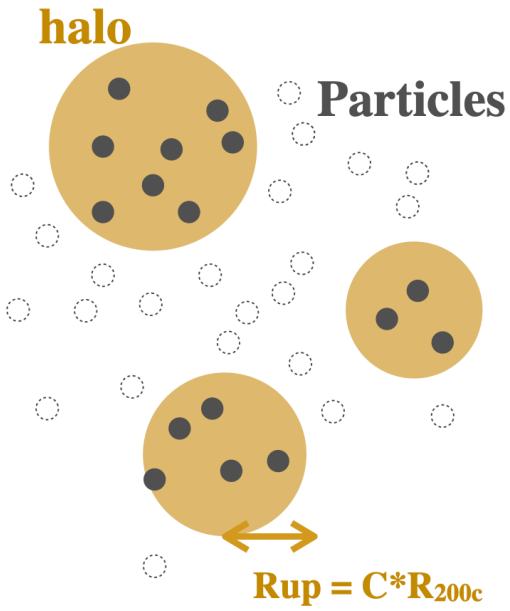

Figure 4.2: A schematic image showing how to create a density field using only the HI inside a sphere with a constant multiple of the halo radius from the halo center. The large yellow circles are a sphere with a constant multiple of the halo radius, the closed black circles represent gas particles inside the sphere, and the open black circles are outside the sphere. The open circles are ignored when creating the HI,so density field.

with 1% accuracy in the range $k < 1h\mathrm{Mpc}^{-1}$. However, for $R_{\mathrm{up}} = R_{200c}$, both amplitude and slope have deviated from the power spectrum with the all HI gas particles. We see that as the radius increases, the power spectrum becomes closer to that using all HI, and for $R = 3R_{\mathrm{up}}$, the difference is less than 1%. This implies that we need to understand the distribution of HI within the halo and around the halo within $R < 3R_{200\mathrm{c}}$.

These results suggest that the contribution of the HI around the halos is non-negligible for the HI power spectrum. Sinigaglia et al. (2021) also shows the importance of the HI other than halo by proposing a method of creating the HI density field by classifying them by their structural characteristics. Therefore, the prescription dealing only with the relation between the halo mass and the HI mass is insufficient and it is important to propose a method for reconstructing the HI density field that includes the surroundings of the halo.

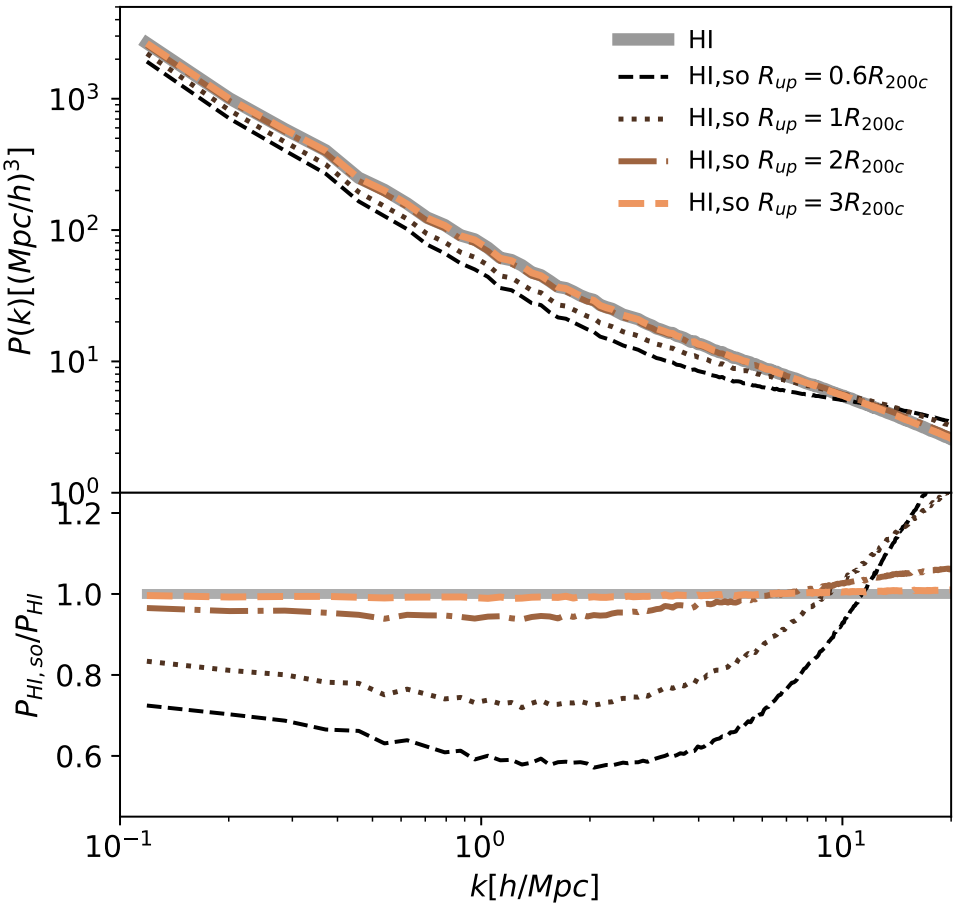

Figure 4.3: Upper panel shows the HI,so power spectrum using gas particles within different halo-centric radii. The other dashed lines are from HI in the vicinity of halos with radii shown in the legend. The total HI power spectrum using all gas particles is also plotted in solid gray line. Bottom panel shows the fractional difference from total HI power spectrum.

Chapter 5

Generate the HI density field and Discussion

We propose a new method to generate the HI density field from the dark matter density field and halos. We aim to measure and model the BAO scale in the HI power spectrum by applying this method to N-body simulations with significant volumes in the future. Furthermore, the BAO analysis will not use the overall amplitude of the power spectrum but only the position of the peaks and troughs. Thus, the target of this method is to create the density field that reproduces the shape of the HI power spectrum at $k \leq 1h\mathrm{Mpc}^{-1}$.

5.1 Spherical Over-density method

In this section, I consider reconstructing the HI distribution from the dark matter particles. If I can reconstruct the HI density field from N-body simulation, this greatly reduces the computational cost. As discussed in section 3.2, the HI is pasted onto dark matter halo using the relation between the halo mass M_{halo} and the HI mass in the halo M_{HI}, which should be calibrated using cosmological hydrodynamic simulations (Villaescusa-Navarro et al., 2018; Sarkar et al., 2016; Sarkar & Bharadwaj, 2018). However, as I shown in 4.2, not only the HI gas within the halos but also those in the vicinity of halos contribute to the HI power spectrum. Furthermore, this method highly depends on the assumed $M_{\mathrm{halo}} - M_{\mathrm{HI}}$ relation, which is measured from hydrodynamic simulation or obtained by using a model with observational data (e.g Wang et al., 2021). Therefore, I propose a more general method (hereinafter called as SO method) for reconstructing the shape of the HI power spectrum which does not rely on the $M_{\mathrm{halo}} - M_{\mathrm{HI}}$ relation.

We test methods in the manner shown in the Fig 5.1. We generate the density field from dark matter particles given by N-body simulation, TNG100-1-Dark. Then I compare the reconstructed power spectrum with the true HI

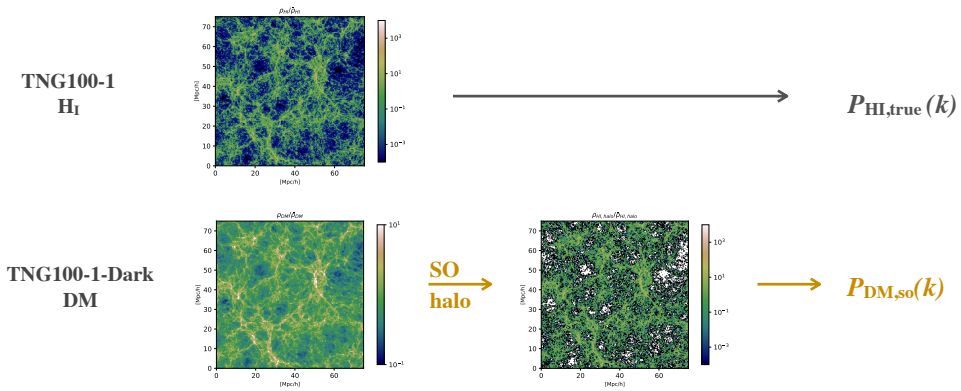

Figure 5.1: Diagram showing how to test the method of creating a HI density field. I compare the reconstructed power spectrum of the DM,so density fields from the N-body simulation with the HI power spectrum computed directly from gas particles in the cosmological hydrodynamic simulation.

power spectrum calculated with the gas particles in TNG100-1 in order to test how well this method reproduce the slope of the HI power spectrum. The SO method generate the HI densitu field in the following process. First, I distinguish between particles that enter the sphere at a distance $R_{\rm up}$ from the center of halo and those that do not. Note that here $R_{\rm up}$ is a constant multiple of the radius of each halo, as in Fig 4.2. Then, I form a density field using only the dark matter particles inside the sphere. In the following, the radius of the sphere is referred to as the truncation radius $R_{\rm up}$.

$$\delta_{\rm DM,so}(\boldsymbol{x}) = \delta_{\rm DM}(\boldsymbol{x}) \times \Theta\left(\sum_i W^{\rm TH}_{R_{\rm up}}(|\boldsymbol{x}-\boldsymbol{x}_i|)\right), \tag{5.1}$$

where index i runs over all halos, x_i denotes the central position of halo, Θ is a step function, $\Theta(X) = 1$ for $X \geq 1$, and 0 otherwise, and $W^{\rm TH}_{R_{\rm up}}$ is a top-hat window function. In this way, I generate a pseudo-scale dependent halo-biased density field (hereinafter called as DM,so density field) by extracting dark matter particles only in and around the halo, and this method uses this density field as the reconstructed HI density field. As a result, the slope of the power spectrum of this density field becomes close to that of the HI power spectrum. For the BAO analysis, the constant amplitude offset of the power spectrum is not important and I only focus on the scale dependence. This form is inspired by the fact that the square of the bias is defined as the ratio of the power spectrum. Then, I define residual function about the ratio to the true power spectrum to quantify how this model reproduces the scale dependence,

$$\mathrm{Res}(k) = \sqrt{P_{\rm HI}/P_{\rm DM,so}}, \tag{5.2}$$

where $P_{\rm DM,so}$ is the reconstructed power spectrum. Then I fit this ratio with linear function of the wavenumber.

$$\mathrm{Res}(k) = b_0 + b_1 k, \tag{5.3}$$

where b_0, b_1 is the coefficient. Since b_1 represents the scale dependency of the ratio, $b_1 = 0$ means the reconstructed power spectrum well reproduces the slope of the HI power spectrum.

By varying the truncation radius, I search for a value at which the b_1 value becomes small. Reconstructed power spectra are shown in Fig 5.2. We see that the 2 times halo radius is best reproduce the slope without the star-forming gas correction.

With the star-forming gas correction, the slope of the HI power spectrum becomes shallower. Therefore, the optimal value of the radius is $0.6R_{\rm up}$, but still does not completely reproduce the slope. I will discuss the change in the HI power spectrum by the correction using a halo model (Seljak, 2000). The halo bias is more significant for massive halos, and the star-forming correction increases the HI gas in particular in massive halos. Therefore, the correction effectively increases the HI bias and the amplitude of the HI power spectrum is boosted on large scales. Also, it is well known that the 2-halo term has a truncation from the linear power spectrum depending on the effective scale of the halo radius. This truncation scale is shifted to a larger scale. This is because the star-forming gas correction selectively increases the HI mass for the massive halos and thus puts more weight on the massive halos. Therefore the effective radius after correction is increased. On the other hand, if we focus on the smaller scales, the contribution of the 1-halo term becomes more significant. Given that the massive halos have larger shot-noise (due to their small number), again, the correction makes the relative contribution from the massive halos more prominent. Thus the amplitude of the 1-halo term also becomes larger. While the increase of the 1-halo term on small scales makes the power spectrum flatter, the shift of the damping scale of the 2-halo term makes it steeper. Therefore, the resulting slope of the power spectrum is determined by the balance of these two competing effects. As a result, the figure 5.2 shows that the slope becomes shallower due to the correction.

These results are valid only at $z = 3$, and I find optimal $R_{\rm up}$ is different at other redshifts. Detail is discussed in Section 5.5.

5.2 Comparing with previous studies

In this section, I compare the SO method with the pasting method that attaches the HI to the dark matter halo. The pasting method requires the relation between the halo mass $M_{\rm halo}$ and the HI mass $M_{\rm HI}$ inside the halo (Wang et al.,

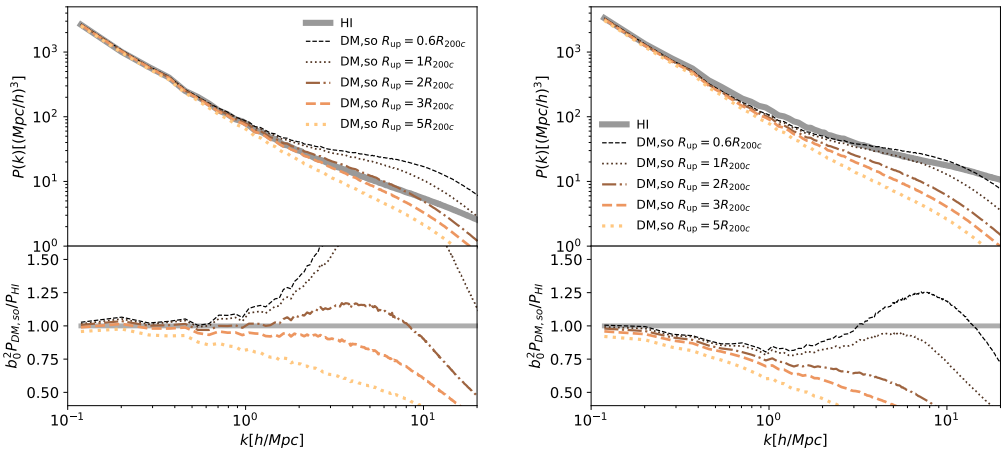

Figure 5.2: *Left panels:* Upper panel shows $b_0^2\, P_{\rm DM,so}(k)$ and the HI power spectrum without the star-forming gas correction. Bottom panel shows the ratio of the reconstructed power spectra to the true HI power spectrum. *Right panels:* Same as the left panels, but with the star-forming gas correction.

2021; Sarkar et al., 2016; Sarkar & Bharadwaj, 2018). Villaescusa-Navarro et al. (2018) shows the 2D-contour of the $M_{\rm halo} - M_{\rm HI}$ relation measured from the IllustrisTNG simulation with star-forming gas correction in Fig 5.3.

In order to compare the pasting method with SO method, I follow the procedures of the pasting method in (Villaescusa-Navarro et al., 2018). For the first step, I fit the following fitting formula with $M_{\rm halo} - M_{\rm HI}$ relation,

$$M_{\rm HI}(M,z) = M_0 \left(\frac{M}{M_{\rm min}}\right)^{\alpha} \exp\left[-\left(\frac{M_{\rm min}}{M}\right)^{0.35}\right], \tag{5.4}$$

where the $M_0, M_{\rm min}, \alpha$ are free parameters and M is a halo mass. This formula is an empirical model describing the relation between the HI and the halo mass, which has low mass cutoff $M_{\rm min}$. To determine the best-fit values, I first divide the halo mass into bins and compute the mean HI mass and variance for each bin. Then I compare the data with the function in Eq 5.4. For each halo, I sum up the HI mass over all FoF gas particles included in that halo. The best-fitting parameters are summarised in Table 5.1 for both with and without star-forming gas correction.

Next, I puts the HI onto center of the dark matter halo in the N-body simulation with the $M_{\rm halo} - M_{\rm HI}$ relation in Eq 5.4. Villaescusa-Navarro et al. (2018) modeled the relation with three parameters ignoring the scatter around this relation, and Modi et al. (2019) argues that including scatter in the pasting method does not significantly change the reconstructed HI power spectrum.

Figure 5.4 shows the ratio of the reconstructed power spectrum using this $M_{\rm halo} - M_{\rm HI}$ relation. Since b_1 represents the scale dependence of the residual

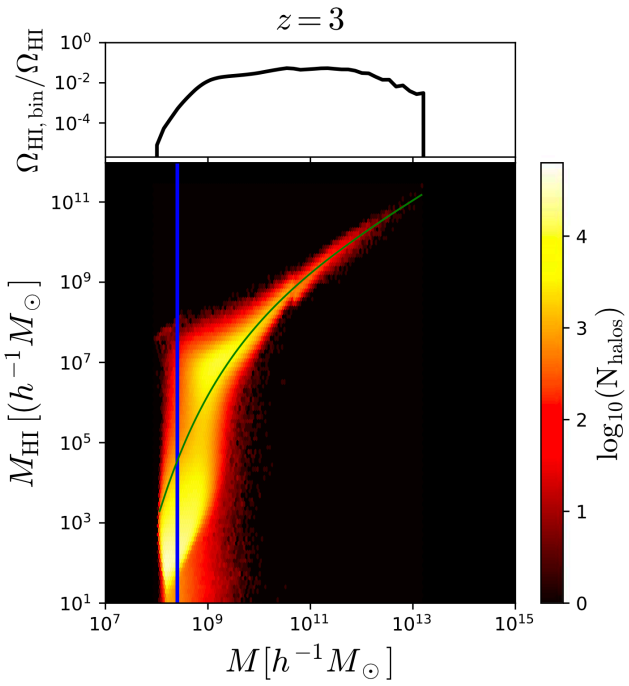

Figure 5.3: The 2D-contour of the halo mass and the HI mass in the halo at $z = 3$ with star-forming gas correction. The horizontal axis is the halo mass, the vertical axis is the HI mass contained therein, and the color indicates the number of halos. Green curve is the best-fitted model for the function in Eq 5.4. This figure is adopted from Villaescusa-Navarro et al. (2018).

Table 5.1: The best-fitting parameters for $M_{\rm halo} - M_{\rm HI}$ relation in Eq 5.4 with and without the star-forming gas correction.

	α	$M_{\rm min}[\rm M_\odot]$	$M_0\,[\rm M_\odot]$
w/ correction	0.82 ± 0.02	$(1.15 \pm 0.07) \times 10^9$	$(3.0 \pm 0.2) \times 10^{10}$
w/o correction	0.54 ± 0.01	$(1.21 \pm 0.06) \times 10^9$	$(4.9 \pm 0.3) \times 10^{10}$

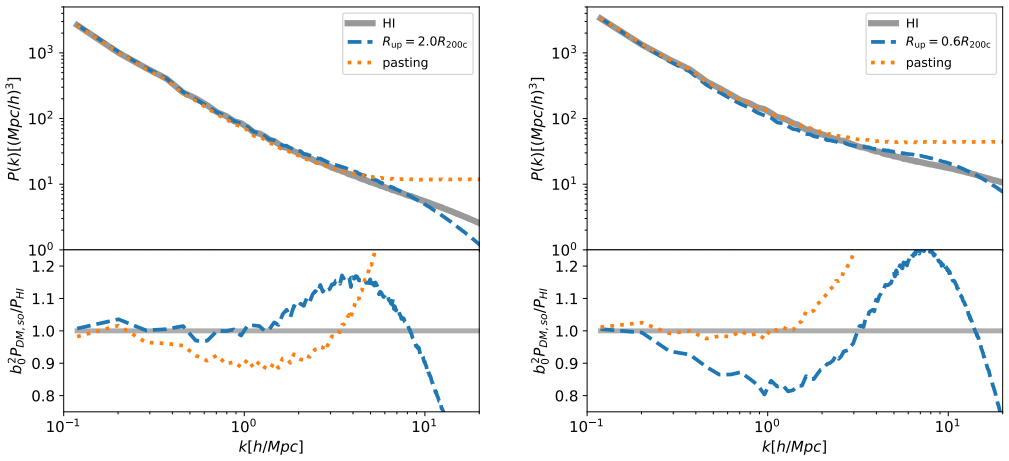

Figure 5.4: *Left panels:* Same as Fig 5.2, but orange-dotted line is the reconstructed from N-body simulation using pasting method and blue-dashed line is that using SO method with $R = 2R_{200c}$. The HI power spectrum is measured from the TNG100-1 without star-forming gas correction (gray solid line). *Right panels:* Same as the left panel, but with the star-forming gas correction.

function in Eq 5.3, we can get how well the slope is reproduced for each model by the b_1 value. Without the correction, $b_1 = 0.07 \pm 0.03$ for the pasting, and $b_1 = 0.005 \pm 0.03$ for the SO method with the radius $R_{\rm up} = 2R_{200c}$. While with the correction, they become $b_1 = 0.01 \pm 0.02$ and 0.16 ± 0.03, respectively. The detail is discussed in Sec 5.5. I find that for the case with the star-forming gas correction the pasting method better reproduce the slope than SO method. On the other hand, without the star-forming gas correction, the SO method is better than the pasting method.

Finally, the SO method has the advantage of simplicity in that only a single parameter $R_{\rm up}/R_{200c}$ for the radius is required to reproduce the HI power spectrum, although with some limitation on the slope of the reconstructed power spectrum with the chosen value of $R_{\rm up}/R_{200c}$. In contrast, the pasting method highly depends on the relation between the $M_{\rm halo} - M_{\rm HI}$ which is sensitive to the resolution of the cosmological hydrodynamic simulation. The HI power spectrum on large scales is mainly contributed from the HI mass inside the halos. Therefore the advantage of the pasting method is that it directly calibrates this relationship from simulations. In addition to the star-forming gas correction, non-trivial astrophysics effects may alter the 21-cm line power spectrum. This means that the reconstruction of the HI power spectrum is subject to the many complex astrophysical effects. Therefore, considering a variety of method for reconstructing the HI power spectrum is essential. The pasting method tells us the HI mass in the halos can well

reproduce the HI power spectrum using $M_{\rm halo} - M_{\rm HI}$ relation. The SO method not only indirectly alters the mass function through the $R_{\rm up}$ but also it takes into account the spatial density distribution in and around the halo. I find those effects are also vital to reconstruct the HI power spectrum.

5.3 Density profile around halo

It is of great interest to see the density profile of the HI within and around the halos both for the cosmological analysis and astrophysical understandings such as baryonic feedback. In section 5.1, we see that the shape of the HI power spectrum is reproduced well using the dark matter halo power spectrum when the halo radius is extended to spedific scales. We will explain how this coincidence came about by shedding light on the difference of density profiles of the dark matter and the HI.

In order to study the density structure of dark matter and gas around the halo, I measured the radial profile of the stacked density for each different halo mass. We first classify all the dark matter and gas particles into FoF or non-FoF (hereinafter called as IGM particles). The radial profile is then measured for each halo to eliminate the effect of neighboring halos at large halo-centric radii. The density profile for IGM particles is also measured separately. I then stack all the halos in the narrow mass bins: For $\log_{10}(M_{\rm halo}[h^{-1}{\rm M}_\odot]) \geq 9$, 10, and 11, the lightest 3000 halos are used, and for $1 \times 10^{12} < M_{\rm halo}[h^{-1}{\rm M}_\odot] < 2 \times 10^{12}$, all halos are used to stack.

Figure 5.5 shows the density profile of the HI and the dark matter for four different halo masses. We see that the HI density changes more rapidly in the radial direction than that of dark matter, and the density gradient is non-zero even at the outside of the halo. In other words, the HI is relatively more concentrated on the halo center and dark matter has more diffuse distribution.

Focusing on the effect of star-forming gas correction, it can be seen that the HI density is increased in the sub-Mpc or Mpc region from the center of the halo. This is consistent with the fact that the star-formation is more effective in the high-density region and the correction increases the neutral fraction. A smaller SO radius is expected to be needed to create such a concentrated density field in the case with the correction. In fact, I have observed that the truncation scale $R_{\rm up}$ is three times smaller for the case with the star-forming gas correction.

Another aspect to answer the aforementioned question is to find a physically motivated scale of the truncation. Recent high-resolution N-body simulations have revealed that there is a clear boundary around the dark matter halo, the so-called splashback radius. Around the splashback radius, the accreting mass reaches the apocenter and is piled up due to low radial velocity (Fillmore & Goldreich, 1984; Bertschinger, 1985; Adhikari et al., 2014;

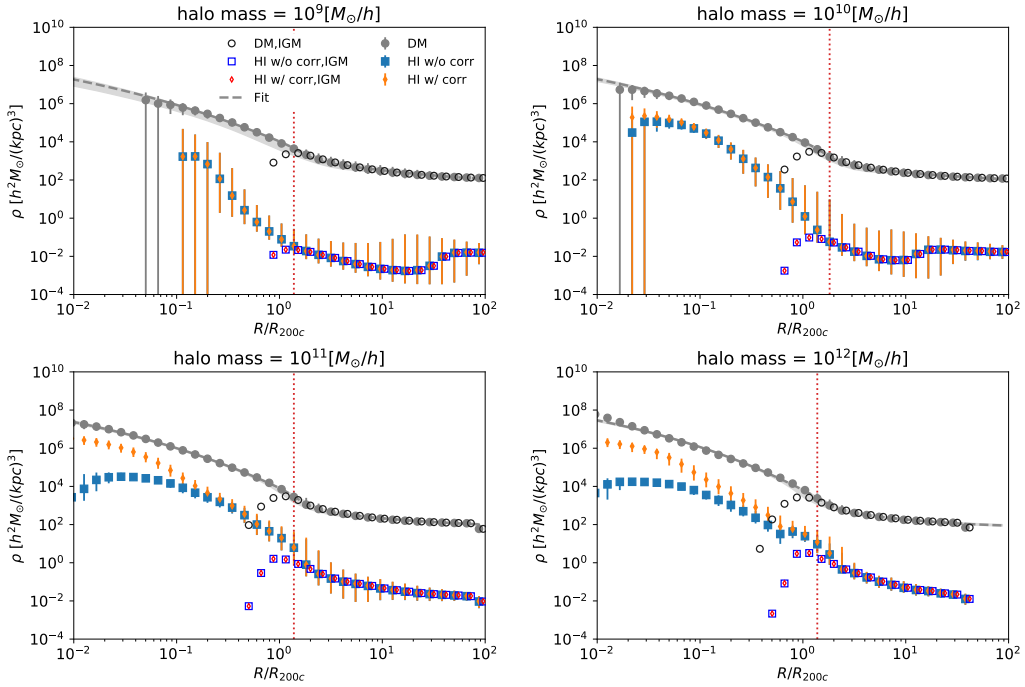

Figure 5.5: Stacked HI and dark matter density profiles for $\log_{10}(M_{\rm halo}[h^{-1}{\rm M}_\odot]) \sim 9$, 10, 11, and 12 from the upper left to the bottom right panel. The grey dashed line shows the best-fitting model for dark matter profile, and the shaded region represents the uncertainty of the fit. For stacking, I use up to the 3000th halo counting from the lower end of the mass $\log_{10}(M_{\rm halo}[h^{-1}{\rm M}_\odot]) \geq 9$, 10 and 11. However for $\log_{10}(M_{\rm halo}[h^{-1}{\rm M}_\odot]) = 12$, I use all halos with masses of $1 \times 10^{12} < M_{\rm halo}[h^{-1}{\rm M}_\odot] < 2 \times 10^{12}$. The vertical dotted red line represents the splashback radius. The open symbols are the profiles measured using only the IGM particles, and the closed ones are those using the FoF and IGM particles. The open symbols are slightly shifted to the right for a better visibility.

Diemer & Kravtsov, 2014; Mansfield et al., 2017). In other words, there is a rapid decline in density just outside the splashback radius, and there is a density gap. Since the probability of finding mass outside the splashback radius is significantly reduced, it seems reasonable to define the truncation scale to be the splashback radius. In practice, the splashback radius is defined as the radius where the logarithmic derivative of the density profile becomes minimum, the steepest point. To measure the splashback radius, I fit the stacked profiles with the following density jump model (Diemer & Kravtsov, 2014):

$$\begin{aligned}
\rho(r) &= f_{\rm trans}\rho_{\rm Einasto} + \rho_{\rm outer}, \\
\rho_{\rm Einasto} &= \rho_s \exp\left(-\frac{2}{\alpha}\left[\left(\frac{r}{r_s}\right)^{\alpha} - 1\right]\right), \\
f_{\rm trans} &= \left[1 + \left(\frac{r}{r_t}\right)^{\beta}\right]^{-\gamma/\beta}, \\
\rho_{\rm outer} &= \rho_m \left[b_e \left(\frac{r}{5R_{\rm 200c}}\right)^{-S_e} + 1\right].
\end{aligned} \tag{5.5}$$

We note that in Diemer & Kravtsov (2014), the outer profile is scaled with $R_{\rm 200m}$, which is the radius where the mean density inside is 200 times the mean density of the Universe. We replace it with $R_{\rm 200c}$ which is used consistently throughout this thesis, and the difference between them are negligibly small in particular at high redshifts. We fix the parameters as $\beta = 6$ and $\gamma = 4$ as in Diemer & Kravtsov (2014); More et al. (2015), and fit the other five parameters within the range of $0.1R_{\rm 200c}$ to $10R_{\rm 200c}$ to the dark matter profiles. Once I find the best-fitting parameters, I differentiate the model to find the splashback radius, $R_{\rm sp}$. For most of the halo masses, the splashback radius is about $1.35R_{\rm 200c}$ and slightly smaller at the massive end, $M \geq 10^{13}h^{-1}{\rm M}_{\odot}$, consistently with More et al. (2015). We denote the ratio as $C(M) \equiv R_{\rm sp}/R_{\rm 200c}$. Finally, I make a density map with the mass-dependent SO radius and $C(M)$, and measured the power spectrum. The scale-dependent terms of the residual function for the splashback radius are $b_1 = 0.03 \pm 0.03$ and $b_1 = 0.27 \pm 0.03$ for the case without and with the star-forming gas correction, respectively. Without star-forming gas correction, the b_1 value is consistent with zero, and larger than the SO method which has $b_1 = -0.005$ at $R_{\rm up}/R_{\rm 200c} = 2$. Since the smaller value of b_1 means better reproduction of the scale dependence of the HI power spectrum on large scales, the splashback radius is a reasonable quantity to use for the case without the star-forming gas correction.

In order to illuminate the individual HI distribution within the halo, Figure 5.6 shows the particles in the FoF halo. The left panel shows the distribution

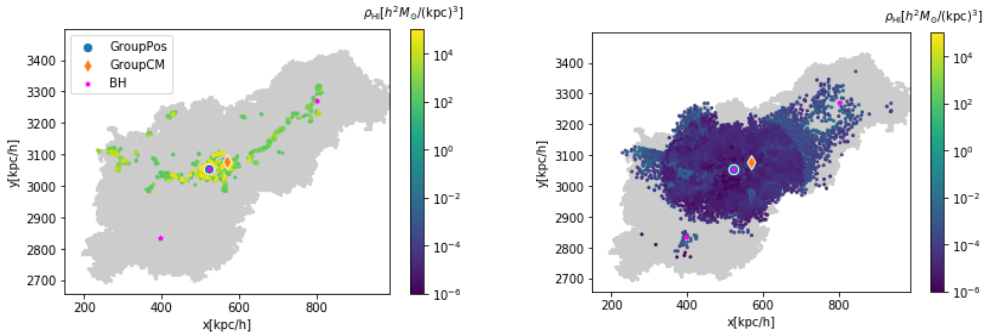

Figure 5.6: *Left panel:* Density distribution of the dark matter (grey points) and HI gas (coloured points) of a certain FoF-halo with a mass of $1.2 \times 10^{12} h^{-1}\mathrm{M}_\odot$. This figure only shows the HI with high densities of $\rho_{\mathrm{HI}} \geq 10^2 h^2 \mathrm{M}_\odot \mathrm{kpc}^{-3}$. The colour gradient shows the value of the HI density. The positions of the halo center, `GroupPos` (blue circle), `GroupCM` (orange diamond), and the black hole (magenta stars) are also plotted. *Right panel:* Same as the left panel but for the lower density HI gas with $\rho_{\mathrm{HI}} \leq 10^{-2} h^2 \mathrm{M}_\odot \mathrm{kpc}^{-3}$.

of the gas particles with high HI density ($\geq 10^2 h^2 \mathrm{M}_\odot \mathrm{kpc}^{-3}$), and the right panel is that with the lower HI density ($< 10^{-2} h^2 \mathrm{M}_\odot \mathrm{kpc}^{-3}$). We also plot the position of the halo center and black holes (BHs) in both panels. As it can be seen from this figure, there is an under-dense region around the BH like a bubble due to AGN feedback. At the same time, we can see the cold flow, a filamentary structure of high density HI around the BH. The halo center, represented by `GroupPos`, overlaps with the position of the BH. The radial density profile in Fig. 5.5 shows that there is a slightly low HI density region around the halo center for the case without the star-formation correction. In other words, the peak of the HI density and the position of the AGN are apart. The recent study on the cross-correlation between Lyman-α absorption and AGNs (Mukae et al., 2020; Momose et al., 2021) also show that there is an under-dense region due to photoionization by the AGN feedback, and the peak of the HI density is a few Mpc away from the position of the AGN. Besides, they also suggest that HI density around the AGN depends on the environments and the AGN type. Hence, the density profile of the HI depends on the astrophysics. Suppose we can determine the effects of astrophysical processes on the HI profile and the HI power spectrum in more detail. In that case, it is expected to constrain the baryonic feedback models by observations of the 21-cm line and the Lyman-α tomography in the future.

5.4 Effect of the spin-temperature fluctuation

In the context of cosmological analysis, the HI power spectrum is the main concern in the literature (Bharadwaj & Pandey, 2005; Sarkar et al., 2016; Sarkar & Bharadwaj, 2018; Padmanabhan & Refregier, 2017; Padmanabhan et al., 2017; Modi et al., 2019). However, what we observe by radio interferometers is the intensity of radio flux or in other words, differential brightness temperature (e.g. Madau et al., 1997; Ciardi & Madau, 2003). In this thesis, I also have neglected the spin temperature fluctuation in the brightness temperature fluctuation under the assumption that the spin temperature is sufficiently higher than the CMB temperature. As shown in Section 3.1 and 4.2, the fluctuations on neutral fraction and gas density and the fluctuation of the spin temperature affect to produce the differential brightness temperature fluctuation. In low-density regions such as voids and inter-galactic medium, the spin temperature may not be sufficiently high, and the spatial fluctuations of the spin temperature may be effective. In this section, I compare the results of the case where only the HI density fluctuations are considered as fluctuations of the brightness temperature and the case where spin temperature fluctuations are also included. The differential brightness temperature fluctuation can be written as follows,

$$\delta T_b \propto \overline{\rho_{\rm HI}}(1+\delta[\rho_{\rm HI}]) \tag{5.6}$$

$$\delta T_b \propto \overline{\rho_{\rm HI} T_{S\gamma}}(1+\delta[\rho_{\rm HI} T_{S\gamma}]), \tag{5.7}$$

where $T_{S\gamma} \equiv (1-T_\gamma/T_S)$. In equation (5.6), $T_{S\gamma}$ is assumed to be unity, which has been considered reasonable at the post-reionization epoch in the literature. On the other hand, in equation (5.7), the spin temperature is also fluctuating in addition to the HI density. Figure 5.7 compares the power spectra defined by equations (5.6) and (5.7) apart from the normalization prefactors. We see that the spin temperature fluctuation causes a slope deviation of about 2% in $k \leq 1h\mathrm{Mpc}^{-1}$. Reminded that the power spectrum at small scales is dominated by high-density regions and large scales by lower density regions. Therefore, the effect of $T_{S\gamma}$ which largely impacts at low-density regions may suppress the amplitude on large scales.

Figure 5.7 also shows the effect of the spin temperature with and without the star-forming gas correction. Since the star-forming gas correction increases HI mass in the high-density region, both the star-forming gas correction and the spin-temperature fluctuations have the effect of weighting the high-density region. Thus, the spin temperature fluctuation is more effective in the case with the star-forming gas correction. Therefore, although the impact of the spin temperature fluctuation varies depending on the treatment of the gas temperature, spin-temperature fluctuations must be taken into account to accurately calculate the 21-cm line power spectrum with an accuracy of a

few percent.

5.5 Evaluate SO method and redshift dependence

We evaluate each model for reconstruction by comparing the reconstructed power spectrum from N-body simulation and the true HI power spectrum from the cosmological hydrodynamic simulation. As introduced in Eq 5.2 and Eq 5.3, I parameterize the model residual as $\sqrt{P_{\rm HI}/P_{\rm Model}} = b_0 + b_1 k$ in order to quantify the degree of deviation of the reconstructed power spectrum. Non-zero b_1 value means that the reconstructed power spectrum has a different slope from the true HI power spectrum.

Figure 5.8 summarises the best-fitting b_1 values at $k \leq 1h{\rm Mpc}^{-1}$. For the case with the star-forming gas correction, we can see that b_1 is consistent with zero in the pasting method, while b_1 value for any radius is inconsistent with zero in the SO method. In contrast, without the star-forming gas correction, the SO method is consistent with zero at $R_{\rm up} = 2R_{200c}$, while the pasting method is inconsistent with zero. In other words, the pasting method well reproduces the slope of the HI power spectrum with the star-forming gas correction, and the SO method well reproduces that without the star-forming gas correction. These results are different when I focus only on the first few peaks and troughs, instead of capturing many BAO peaks and troughs. Figure 5.9 is same as Fig. 5.8 but using only scales $k \leq 0.3h{\rm Mpc}^{-1}$ for fitting the residual. The results are consistent with zero within the standard deviation at all SO radii, both with and without the star-forming gas correction. However, it should be noted that this is partly due to the significant error caused by the smaller number of modes on the large scales. In the future, we need to measure the BAO scale with 1% accuracy, which requires $\sigma_{b_1} \leq 0.01$. To achieve this, a simulation with a box size of $500h^{-1}{\rm Mpc}$ is required.

We also investigate the redshift dependence of the optimal $R_{\rm up}$. Figure 5.10 shows the b_1 values at $z = 0.5, 1$ and 3. We see that the b_1 monotonically increases from $z = 0.5$ to 3, and thus the optimal $R_{\rm up}$ decreases. The increase of b_1 is explained by the difference in the way of non-linear evolution of the power spectra between DM,so and HI. Figure 5.11 shows the growth of the power spectrum from $z = 3$ to $z = 0.5$. We see that the matter power spectrum grows at the linear growth rate, $(D(z = 0.5)/D(z = 3))^2$, on large scales. On small scales, the growth of the matter power becomes strong due to the non-linear growth of gravity. On the other hand, the growth of the DM,so power spectrum is smaller than that of the linear growth of the matter power. This is because it is suppressed by the halo bias evolution, given that the halo is a less-biased tracer at low redshifts. Interestingly the non-linear boost of the DM,so is similar to that of the matter power spectrum, presumably because the matter still exists in the IGM at $z = 3$ and will be accreted

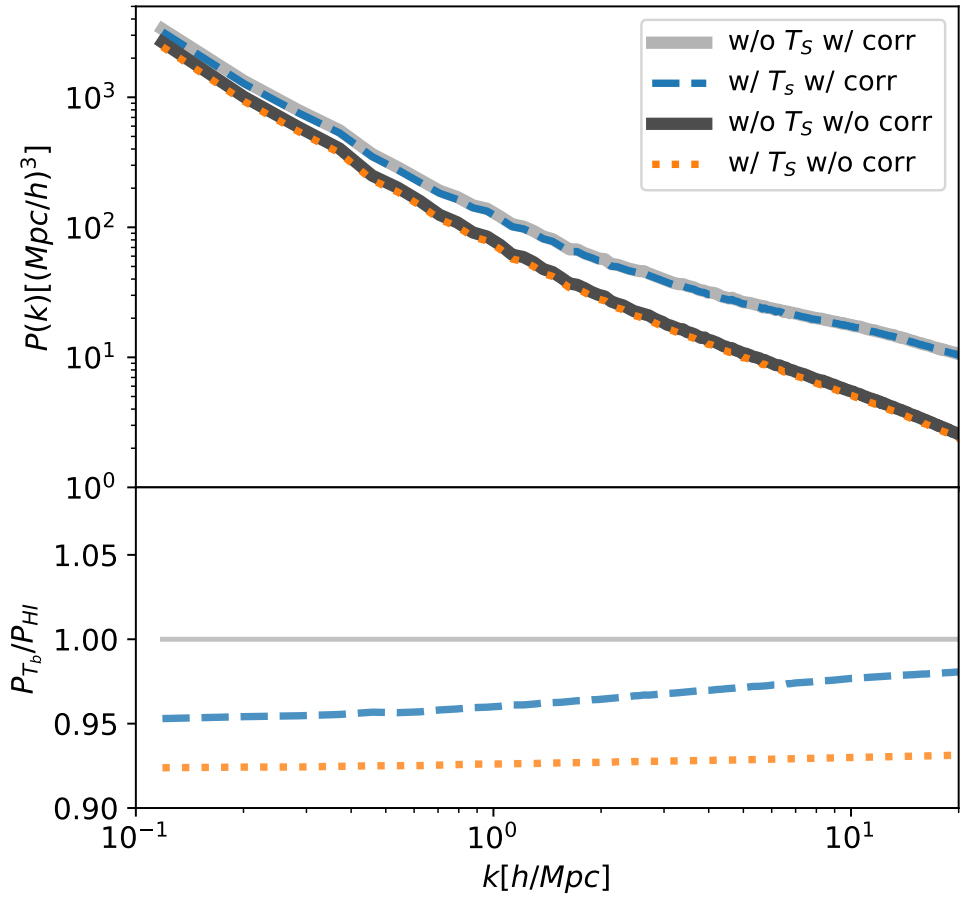

Figure 5.7: Comparing the HI power spectrum $P_{\rm HI}(k)$ (solid line) and the brightness temperature power spectrum $P_{T_b}(k) = P_{n_{\rm HI}(1-T_\gamma/T_S)}(k)$ without (orange dashed line) and with the star-forming gas correction (blue dashed line). Thick light grey curve is the HI power spectrum $P_{\rm HI}(k)$ with the star-forming gas correction and the thick dark grey curve is that without the correction.

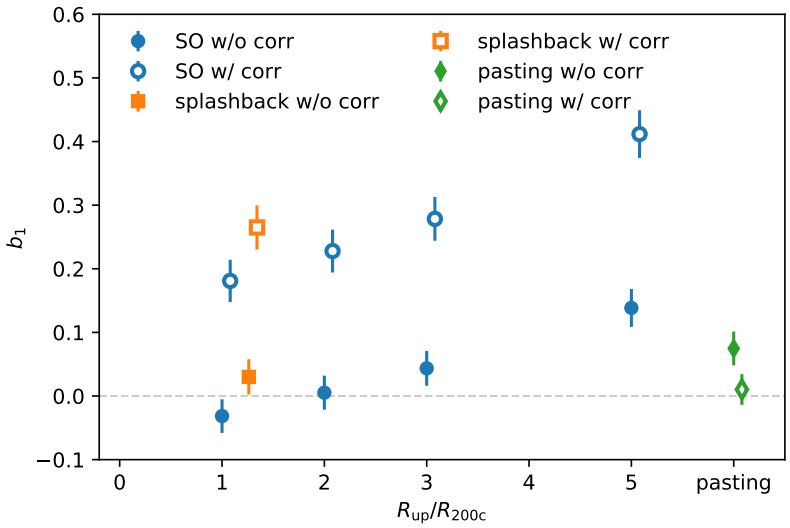

Figure 5.8: Best-fitting parameters of the scale-dependent term b_1 for $k < 1h\mathrm{Mpc}^{-1}$ in Eq. 5.3 for the cases using the SO radius (blue circles), pasting (green diamonds), and splashback radius (orange squares). Closed symbols are the case without the star-forming gas correction and open symbols are that with the correction. The horizontal line of $b_1 = 0$ means that there is no scale-dependent bias.

onto halos. We also see that the growth of the HI power spectrum is smaller than that of DM,so for $k < 1h^{-1}\mathrm{Mpc}$. This is because most of the hydrogen in the IGM has already been ionized at $z = 3$. In other words, most of the HI is already confined within the halos. Thus, for $k \leq 0.1h\mathrm{Mpc}^{-1}$, the scale dependence of growth for the DM,so is stronger than that for HI. It makes the residual function more scale-dependent at low redshift, and b_1 has a large negative value at $z = 0.5$.

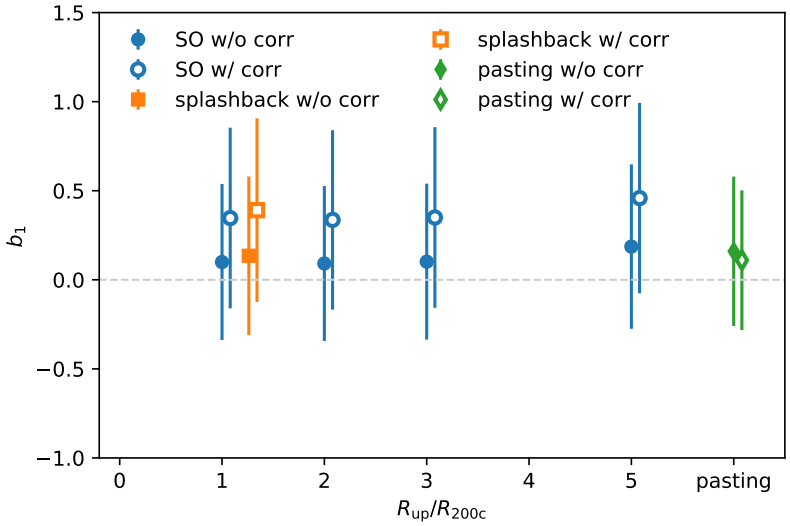

Figure 5.9: Best-fitting parameters of the scale-dependent term b_1 obtained using only the first three points of the power spectrum on the large scales $k < 0.3h\mathrm{Mpc}^{-1}$.

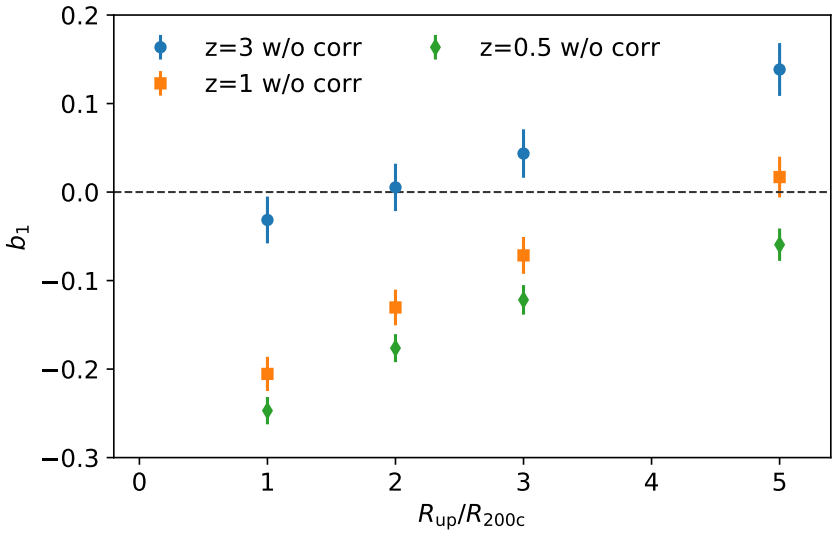

Figure 5.10: Redshift evolution of the best-fitting parameters of the scale-dependent term b_1 for $k < 1h\mathrm{Mpc}^{-1}$. Green diamond, orange square, and blue circle are for $z = 0.5, 1$, and 3, respectively.

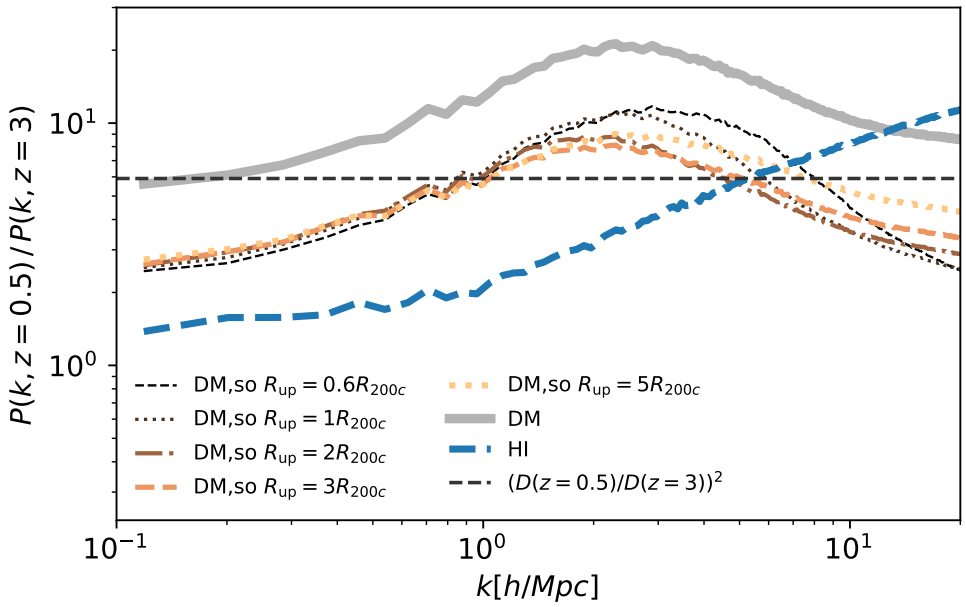

Figure 5.11: The ratio of the power spectrum at $z = 0.5$ and $z = 3$. Gray solid line is for the dark matter power spectrum, and blue dashed line is for the HI without the star-forming gas correction. Other lines are the DM,so with different $R_{\rm up}$. The horizontal dashed line represents the linear growth rate from $z = 3$ to $z = 0.5$.

Chapter 6

Summary and Conclusion

Although dark energy is thought to be the origin of the accelerated expansion of the Universe, it is not clearly understood. The equation of state parameter is a quantity that characterizes dark energy, and there are various models such as constant and time-varying. Measuring the equation of state parameters leads to a constraint on dark energy.

In recent years, BAO has been used to constrain dark energy. Since BAO is a standard ruler of the Universe, we can measure the expansion history and distance by BAO measurement. Since different dark energy models bring different expansion histories, BAO measurement is useful for constraints on dark energy. Since electromagnetic waves cannot capture dark matter, BAO measurements by galaxy surveys have often been performed. Now the HI is attracting attention as a new tracer of dark matter. In fact, the 21-cm IM by SKA will start at 2020s. The 21-cm line IM has several advantages. One is that the redshift of an the object can be identified from its frequency. Second, the 21-cm IM observes the 21-cm intensity field without resolving individual galaxies, making it possible to explore more distant and wider regions than conventional surveys. This will allow us to understand the time evolution of galaxies from the past and expect it to provide a strong constraint on dark energy.

However, because of the discrepancy between the HI and DM distributions, the position of the BAO wiggle in the HI power spectrum is expected to deviate from the theoretical prediction for DM. In addition, the time evolution of the HI density field is affected by the UV background radiation and feedback from stars and galaxies, which makes it difficult to calculate analytically. Therefore, the ultimate goal of this study is to construct a framework for comparing 21-cm line observations with theory using simulations for the future 21-cm IM surveys. Ando et al. (2019); Villaescusa-Navarro et al. (2018) has already measured the HI bias and tested RSD models using cosmological hydrodynamic simulation. However, to model the deviation of the BAO scales more accurately, we need the simulation with larger box size. In order

to measure the power spectrum at large scales with small errors, a large number of k modes is required, as can be seen in Eq 4.2. Therefore we need the simulation with large box size. Therefore, for the BAO analysis, a simulation with a box size of 75 Mpc is not sufficient, and a larger simulation with a size of 500 Mpc or more is needed. Moreover, cosmological hydrodynamic simulations strongly depend on particle resolution, but high-resolution simulations are computationally expensive. Then, the quasi-analytical methods are used in the literature, they first compute the growth of the dark matter from N-body simulation and then create the HI density field. Since most of the HI after the reionization epoch exists inside the halo, Sarkar et al. (2016); Sarkar & Bharadwaj (2018); Modi et al. (2019); Wang et al. (2021) use the method of pasting the HI onto the dark matter halo. However, this method depends on the relationship between the halo and HI mass in the halo. In addition, it is necessary to verify whether it is sufficient to consider only the HI inside the halo.

In this thesis, I propose a new method to create the HI density field from the dark matter density field for the BAO analysis. Specifically, I construct a method that reproduces the slope of the HI power spectrum obtained from cosmological hydrodynamic simulation. In this thesis, I used TNG100-1, which is cosmological hydrodynamic simulation, and TNG100-1-Dark, which is an N-body simulation and has the same initial conditions as TNG100-1. We performed our analysis in the real space at redshift 3.

This thesis first use TNG100-1 to investigate how much the HI in and around the halos affects the power spectrum in chapter 4. As a result, the HI inside a sphere at a halo radius contributes about 80%, and the HI within three times the radius gives 99% of the contribution to the HI power spectrum. This means that the HI power spectrum is determined only by the HI inside and near the halo.

In Chapter 5, I proposed a method to create HI distributions from the DM density field in TNG100-1-Dark. First, I create a density field using only DM particles inside a sphere of constant times the halo radius. Then, I compare the power spectrum from that density field with the true HI power spectrum, which is calculated from the gas particles in TNG100-1. We repeat this process for different radii to find the optimal radius that best reproduces the slope of the power spectrum. As a result, it was found that $R_{\rm up} = 2R_{200c}$ best reproduce the shape. On the other hand, I did the same analysis with a star-forming gas correction. The star formation activity is high in the massive halos and this correction increases the HI mass by fixing the temperature of the star-forming gas particles to 10^4K. Consequently, the HI bias becomes high, and the slope becomes gentle. As a result, any radius does not reproduce

the tilt well, and the optimal radius is 0.6 times the halo radius.

We then compare the radial density profiles around the halo for dark matter and the HI. I found that the HI is more concentrated near the halo center than DM but the HI is still distributed even outside the halo radius. We also find that the star-forming gas correction increases the HI density at the center of the halo. This is consistent with the fact that the SO radius $R_{\rm up}$ becomes smaller when the correction was included in Chapter 5.

We have been analyzing the 21-cm line power spectrum assuming that the spatial fluctuation of the spin temperature is negligible after the reionization epoch. However, strictly speaking, the effect of the spin temperature may not be negligible due to the lower gas temperature in the low-density region. We analyzed the effect of the spin temperature fluctuations on the 21-cm line power spectrum using TNG100-1. I found that it affects the amplitude and the slope of the 21-cm line power spectrum by 8% and 2%, respectively, at most.

In addition to the fiducial analysis at $z = 3$, I performed this analysis for $z = 0.5$ and 1 as well, and find that the SO radius depends on the redshift. The SO radius decreases with higher redshift. This is consistent with the result that the scale dependence of the HI bias becomes higher at high redshift and the HI power spectrum is higher at small scales (Ando et al., 2019).

We also compared this SO method with the pasting method, which pastes HI to the DM halo center using Halo and HI mass relation. SO method reproduces the tilt better in the case without the star-forming gas correction. In contrast, the pasting method reproduces it better with the correction. Although the SO method reproduces the inclination with a single parameter about a radius, it was found that which method reproduces it better depends on the treatment of the HI gas and redshift.

Future 21-cm line IM by SKA are expected to measure the BAO scales with an accuracy of 1%. Therefore, we will require the simulation with $500h^{-1}\mathrm{Mpc}$ or larger box sizes. In the future, the method proposed in this thesis can be adapted to the N-body simulations that have significant box-size and high mass resolution to create the HI density fields that can precisely discuss the BAO scales.

Bibliography

Adhikari S., Dalal N., Chamberlain R. T., 2014, J. Cosmology Astropart. Phys., 2014, 019

Anderson C. J., et al., 2018, MNRAS, 476, 3382

Ando R., Nishizawa A. J., Hasegawa K., Shimizu I., Nagamine K., 2019, MNRAS, 484, 5389

Aoyama S., Hou K.-C., Hirashita H., Nagamine K., Shimizu I., 2018, MNRAS, 478, 4905

Ata M., et al., 2018a, MNRAS, 473, 4773

Ata M., et al., 2018b, MNRAS, 473, 4773

Bernardeau F., Colombi S., Gaztañaga E., Scoccimarro R., 2002, Phys. Rep., 367, 1

Bertschinger E., 1985, ApJS, 58, 39

Beutler F., et al., 2011, MNRAS, 416, 3017

Bharadwaj S., Pandey S. K., 2005, MNRAS, 358, 968

Bowman J. D., Rogers A. E. E., Monsalve R. A., Mozdzen T. J., Mahesh N., 2018, Nature, 555, 67

Chang T.-C., Pen U.-L., Bandura K., Peterson J. B., 2010, arXiv e-prints, p. arXiv:1007.3709

Ciardi B., Madau P., 2003, ApJ, 596, 1

Colless M., 1999, Philosophical Transactions of the Royal Society of London Series A, 357, 105

Crighton N. H. M., et al., 2015, MNRAS, 452, 217

Diemer B., Kravtsov A. V., 2014, ApJ, 789, 1

Drinkwater M. J., et al., 2010, MNRAS, 401, 1429

Dubois Y., Peirani S., Pichon C., Devriendt J., Gavazzi R., Welker C., Volonteri M., 2016, MNRAS, 463, 3948

Eisenstein D. J., et al., 2005, ApJ, 633, 560

Faucher-Giguère C.-A., Lidz A., Zaldarriaga M., Hernquist L., 2009, ApJ, 703, 1416

Fillmore J. A., Goldreich P., 1984, ApJ, 281, 1

Friedmann A., 1922, Zeitschrift fur Physik, 10, 377

Genel S., et al., 2014, MNRAS, 445, 175

Gil-Marín H., et al., 2020, MNRAS, 498, 2492

Hubble E., 1929, Proceedings of the National Academy of Science, 15, 168

Hui L., Gnedin N. Y., 1997, MNRAS, 292, 27

Krumholz M. R., McKee C. F., Tumlinson J., 2008, ApJ, 689, 865

Krumholz M. R., McKee C. F., Tumlinson J., 2009, ApJ, 693, 216

Lah P., et al., 2007, MNRAS, 376, 1357

Lemaître G., 1927, Annales de la Société Scientifique de Bruxelles, 47, 49

Lepori F., Di Dio E., Viel M., Baccigalupi C., Durrer R., 2017, J. Cosmology Astropart. Phys., 2017, 020

Madau P., Meiksin A., Rees M. J., 1997, ApJ, 475, 429

Makinen T. L., Lancaster L., Villaescusa-Navarro F., Melchior P., Ho S., Perreault-Levasseur L., Spergel D. N., 2021, J. Cosmology Astropart. Phys., 2021, 081

Mansfield P., Kravtsov A. V., Diemer B., 2017, ApJ, 841, 34

Marinacci F., et al., 2018, MNRAS, 480, 5113

Masui K. W., et al., 2013, ApJ, 763, L20

McKee C. F., Krumholz M. R., 2010, ApJ, 709, 308

Mesinger A., Furlanetto S., Cen R., 2011, MNRAS, 411, 955

Modi C., Castorina E., Feng Y., White M., 2019, J. Cosmology Astropart. Phys., 2019, 024

Momose R., et al., 2021, ApJ, 909, 117

More S., Diemer B., Kravtsov A. V., 2015, ApJ, 810, 36

Mukae S., et al., 2020, ApJ, 896, 45

Naiman J. P., et al., 2018, MNRAS, 477, 1206

Nelson D., et al., 2015, Astronomy and Computing, 13, 12

Nelson D., et al., 2018, MNRAS, 475, 624

Nelson D., et al., 2019, Computational Astrophysics and Cosmology, 6, 2

Noterdaeme P., et al., 2012, A&A, 547, L1

Padmanabhan H., Refregier A., 2017, MNRAS, 464, 4008

Padmanabhan H., Refregier A., Amara A., 2017, MNRAS, 469, 2323

Parsons A., et al., 2019, in Bulletin of the American Astronomical Society. p. 241 (arXiv:1907.06440)

Peebles P. J. E., Yu J. T., 1970, ApJ, 162, 815

Perlmutter S., et al., 1999, ApJ, 517, 565

Piattella O. F., 2018, arXiv e-prints, p. arXiv:1803.00070

Pillepich A., et al., 2018a, MNRAS, 473, 4077

Pillepich A., et al., 2018b, MNRAS, 475, 648

Planck Collaboration et al., 2016, A&A, 594, A13

Planck Collaboration et al., 2020, A&A, 641, A6

Pritchard J. R., Loeb A., 2012, Reports on Progress in Physics, 75, 086901

Rahmati A., Pawlik A. H., Raičević M., Schaye J., 2013, MNRAS, 430, 2427

Rao S. M., Turnshek D. A., Nestor D. B., 2006, ApJ, 636, 610

Riess A. G., et al., 1998, AJ, 116, 1009

Ross A. J., Samushia L., Howlett C., Percival W. J., Burden A., Manera M., 2015, MNRAS, 449, 835

Santos M., et al., 2015, in Advancing Astrophysics with the Square Kilometre Array (AASKA14). p. 19 (arXiv:1501.03989)

Sarkar D., Bharadwaj S., 2018, MNRAS, 476, 96

Sarkar D., Bharadwaj S., Anathpindika S., 2016, MNRAS, 460, 4310

Schaye J., et al., 2015, MNRAS, 446, 521

Seljak U., 2000, MNRAS, 318, 203

Shimizu I., Todoroki K., Yajima H., Nagamine K., 2019, MNRAS, 484, 2632

Sijacki D., Vogelsberger M., Genel S., Springel V., Torrey P., Snyder G. F., Nelson D., Hernquist L., 2015, MNRAS, 452, 575

Sinigaglia F., Kitaura F.-S., Balaguera-Antolínez A., Nagamine K., Ata M., Shimizu I., Sánchez-Benavente M., 2021, ApJ, 921, 66

Songaila A., Cowie L. L., 2010, ApJ, 721, 1448

Springel V., 2010, MNRAS, 401, 791

Springel V., Hernquist L., 2003, MNRAS, 339, 289

Springel V., et al., 2018, MNRAS, 475, 676

Square Kilometre Array Cosmology Science Working Group et al., 2020, PASA, 37, e007

Staveley-Smith L., et al., 1996, PASA, 13, 243

Switzer E. R., Chang T. C., Masui K. W., Pen U. L., Voytek T. C., 2015, ApJ, 815, 51

Tanaka T., Hasegawa K., Yajima H., Kobayashi M. I. N., Sugiyama N., 2018, MNRAS, 480, 1925

Villaescusa-Navarro F., et al., 2018, ApJ, 866, 135

Vogelsberger M., et al., 2014a, MNRAS, 444, 1518

Vogelsberger M., et al., 2014b, Nature, 509, 177

Wang Z., et al., 2021, ApJ, 907, 4

Wolz L., et al., 2017, MNRAS, 464, 4938

Wouthuysen S. A., 1952, AJ, 57, 31

Wyithe J. S. B., Loeb A., 2008, MNRAS, 383, 606

Zamudio-Fernandez J., Okan A., Villaescusa-Navarro F., Bilaloglu S., Derin Cengiz A., He S., Perreault Levasseur L., Ho S., 2019, arXiv e-prints, p. arXiv:1904.12846

Zarrouk P., et al., 2021, MNRAS, 503, 2562

du Mas des Bourboux H., et al., 2020, ApJ, 901, 153